CONF-741003

Precipitation Scavenging (1974)

Proceedings of a symposium held at
Champaign, Illinois
October 14–18, 1974

Sponsored by

Illinois State Water Survey

and

Division of Biomedical and Environmental Research
U. S. Atomic Energy Commission

Coordinators

Richard G. Semonin
Illinois State Water Survey

Robert W. Beadle
U. S. Atomic Energy Commission

1977

Published by
Technical Information Center
Energy Research and Development Administration

A PRECIPITATION SCAVENGING MODEL FOR NUCLEAR FALLOUT RESEARCH

H. G. NORMENT*
Mt. Auburn Research Associates, Newton, Massachusetts

ABSTRACT

A precipitation scavenging capability has been developed for the DELFIC fallout prediction code. The DELFIC Precipitation Scavenging Module (PSM) consists of:

1. A kinematic storm-cloud circulation model.
2. Cloud microphysics models for water and ice.
3. Aerosol scavenging models.

Atmospheric transport of nuclear cloud particles into the storm and transport of scavenged particles (as hydrometeor–particle combinations) from the cloud are accomplished with a modified DELFIC transport calculation. The microphysics models are based on Kessler's parameterizations for water and Koenig's parameterizations for ice.

Scavenging is by the following mechanisms:

1. *Below-cloud:* Inertial collection by precipitation.
2. *In-cloud:* (a) Nucleation and condensation growth of water drops or ice crystals coincident with inertial collection of the growing particles by precipitation, and (b) Brownian scavenging by cloud-water drops coincident with inertial collection of the cloud water by precipitation.

Phoretic scavenging is not included because it is too slow to lead to militarily significant, local, ground deposition of fallout.

Calculations for a rainstorm that yields 20 mm hr^{-1} precipitation at the ground indicate a below-cloud aerosol scavenging threshold between 1.5 and 2.0 μm in diameter. An in-cloud threshold of 0.3 μm is indicated. Calculations for a snowstorm that yields 10 mm hr^{-1} precipitation at the ground indicates similar results below cloud but an in-cloud threshold of $\sim$0.02 μm. Interactions of nuclear and storm clouds are discussed. Intermediate scavenging results and final ground-deposition results are presented.

Under dry-air conditions the finely divided, highly radioactive aerosol produced by a nuclear airburst poses no immediate threat to tactical

* Present affiliation: Atmospheric Science Associates, Bedford, Mass.

military operations. Moreover, from 15 to 40% of the total radioactivity produced by a surface burst may reside in particles too small to be deposited locally. However, interaction of a nuclear cloud with a natural precipitating cloud can radically alter this picture owing to precipitation scavenging effects.

The objective of the work reported here is to develop a model that can be used to assess the significance of precipitation scavenging to tactical military operations under a variety of realistic field conditions. Emphasis has been put into development of microphysics and scavenging models. Some compromise of rigor has been necessary to cope with meteorological complexities at the macroscale and mesoscale levels in the way these affect storm-cloud and atmospheric transport hydrodynamics.

The DELFIC fallout prediction system[1-5] is used to handle nuclear cloud rise, atmospheric transport exterior to the storm cloud, and processing of ground-deposited debris into radiation exposure rate or dose maps. The new scavenging model in DELFIC is called the Precipitation Scavenging Module (PSM).

THE DELFIC FALLOUT PREDICTION SYSTEM

The DELFIC (Refs. 1 to 5) is a research-oriented code designed to predict transport and local deposition of nuclear debris. The range of deposition will vary from several miles to several hundred miles, depending on the size of the nuclear explosion. Explosion yields from 0.01 kT to 25 MT are accommodated. In prior versions DELFIC was limited to surface or near-surface bursts. Along with the addition of the PSM, the capability of the DELFIC is extended to airbursts. It can simulate precipitation scavenging of debris from surface and airbursts and deposition of wet and/or dry fallout.

The nuclear cloud rise model of DELFIC is based on the dynamic, entraining, turbulent-bubble model of Huebsch.[6] The model accounts for effects of explosion yield, altitude of burst and height of burst above ground, soil and water loading, water condensation effects, atmospheric stability, and wind shear. The cloud rise simulation defines the composition of the nuclear cloud at stabilization time in terms of a spatial distribution of monodisperse parcels of debris. The complete set of parcels represents a composite of the cloud. This composite contains as much resolution detail, with respect to both space and particle size distributions, as is desired by the user.

The Diffusive Transport Module (DTM) accepts three-dimensional wind and turbulence data that can be space and time resolved as befits the demands of the problem under study. Turbulent dispersion of fallout

in the horizontal can be simulated with the Batchelor–Kolmogoroff similarity theory[7,8] or with the simple Fickian diffusion. Effects of mixing-layer turbulence on fallout deposition can be accounted for when necessary.

For surface bursts, DELFIC assigns radioactivity to fallout particles by a modified version of the Freiling radial distribution model.[9] Three sources of radioactivity are considered: (1) fission products; (2) products of the n,γ reaction on ^{238}U in the device; and (3) neutron-induced activity in the soil. The model computes the decay of each individual nuclide from the time of detonation to any subsequent time by the Bateman equation.[10] For airbursts, activity is computed from a "K-factor" [total H + 1 hr exposure rate for 1 kT of fission products 3 ft above an infinite plane concentrated in $1m^2$, roentgens (R) $hr^{-1}/kT\ m^{-2}$].[11] A $t^{-1.26}$ activity decay law is used. There is little known about the distribution of activity with debris particle size for airbursts. To obtain the results presented here, I assume that activity is distributed in proportion to particle volume.

Ground-deposited fallout is processed into any or all of 16 unique map displays.[5] The map display options include fallout mass per unit area, exposure rate "normalized" to H + 1 hr, exposure rate at any specified time, exposure integrated over any specified time interval, mass per unit area contributed by a specified particle size range, time of onset of fallout, time of cessation of fallout, smallest particle size deposited, and largest particle size deposited. Map boundaries and grid intervals are set by the user.

STORM-CLOUD CIRCULATION KINEMATICS

The PSM is an integral part of the DELFIC Diffusive Transport Module (DTM). The DTM provides a "background" wind field that presumably would exist in the absence of the storm. These winds are defined at the centers of cells in a three-dimensional space grid. The storm is localized within this grid. The DTM transports parcels of debris particles into and/or around the storm cloud. It was not possible, or even particularly desirable, to add a dynamic storm-cloud capability to DELFIC. For an account of circulation effects of the storm, both exterior and interior to the cloud, a kinematic cloud circulation model was developed. The total wind field is obtained by adding the storm winds to the background winds. Although it is not rigorously correct to simply add independently determined winds in this fashion, overall trends should be adequately simulated.

In a pioneering cloud microphysics paper, Wexler and Atlas[12] summarize evidence that vertical storm-cloud air flux is an approximate parabolic function of pressure. On this basis Kessler[13] also used such

a model of air flux in his exploratory microphysics studies. Whereas these studies were concerned with in-cloud updrafts, I require a three-dimensional model that extends to the cloud exterior. In addition, a serious disadvantage of the parabolic model is that the flux changes sign at or near the cloud top.

I have developed an exponential approximation to the parabolic vertical flux model. This approximation maintains the effect of the ground boundary, and it approaches zero flux asymptotically but rapidly above the cloud top. The model also provides for horizontal flow both interior and exterior to the cloud.

Assume an axially symmetric steady-state storm cloud and ignore local variations of air density except in the vertical. The continuity equation is

$$\frac{1}{r}\frac{\partial(rU)}{\partial r} + \frac{\partial w}{\partial z} = -\frac{w}{\rho}\frac{\partial \rho}{\partial z} \tag{1}$$

The symbols used are defined in Appendix 1. With the additional assumption of a hydrostatic atmosphere, $dP/dz = -\rho g$, Eq. 1 reduces to

$$\frac{1}{r}\frac{d(rU)}{dr} = g\frac{d(w\rho)}{dP} \tag{2}$$

Since the variables are separable, we can devise solutions for U and $w\rho$ with independent consideration of the desired properties of these quantities.

These properties are:

A. For vertical flux ($w\rho$)
   1. Zero at the ground.
   2. Positive interior to and above the cloud.
   3. Within a horizontal plane at specified altitude, the maximum is on the cloud axis.
   4. Negative but small beyond the horizontal cloud boundary.
   5. Approximate parabolic function of pressure inside the cloud, with maximum at the barometric center of the cloud.
   6. Rapid asymptotic approach to zero above the cloud.
   7. Somewhat more gradual asymptotic approach to zero beyond the horizontal cloud boundary.

B. For horizontal velocity (U)
   1. Zero at the cloud center.
   2. Convergent toward the cloud axis below the barometric center of the cloud and divergent above.

3. Along a horizontal axis at fixed altitude, the maximum magnitude should be near the cloud boundary.
4. Rapid asymptotic approach to zero above the cloud.
5. Somewhat more gradual asymptotic approach to zero beyond the horizontal cloud boundary.

A solution that fits these requirements is

$$\frac{w\rho}{(w\rho)_{max}} = e^{1/3}\,\zeta(1-\eta^2)\exp\left(-\frac{\zeta^3}{3}-\eta^2\right) \tag{3}$$

$$\frac{U}{|U_{max}|} = -(2e)^{1/2}\,\eta(1-\zeta^3)\exp\left(-\frac{\zeta^3}{3}-\eta^2\right) \tag{4}$$

where

$$\zeta = 2\frac{P_0 - P}{P_0 - P_T} \tag{5}$$

$$\eta = \frac{r}{\Phi} \tag{6}$$

$$U_{max} = -\frac{g(w\rho)_{max}\Phi}{(2)^{1/2}\,e^{1/6}\,(P_0 - P_T)} \tag{7}$$

and P_0 and P_T are pressure at the ground and cloud top, respectively. The stream function for the cloud circulation is

$$\psi = -\frac{1}{2}\Phi^2\,(w\rho)_{max}\,\zeta\eta^2\exp\left(\frac{1-\zeta^3}{3-\eta^2}\right) \tag{8}$$

For a stratus cloud we let the horizontal cloud boundary extend to infinity; then $U = 0$ and Eq. 3 becomes

$$\frac{w\rho}{(w\rho)_{max}} = \zeta\exp\left[\frac{1}{3}(1-\zeta^3)\right] \tag{9}$$

As used in DELFIC, the interior of a cumulus storm is confined to a vertical tier of space cells. The wind vector is held constant throughout each cell. Accordingly, the updraft in a cell is taken as the horizontal-area-weighted-average updraft flux computed in the mid-level plane of the cell. Thus

$$\overline{\rho w} = 2\rho \int_0^1 w\eta d\eta$$

from which we obtain

$$\bar{w} = \frac{(w\rho)_{max}}{\rho} \zeta \exp\left[-\frac{1}{3}(2 + \zeta^3)\right] \tag{10}$$

Figure 1 shows an illustrative example of a cumulus cloud, and Figs. 2 and 3 show updraft structures for two case studies.

STORM-CLOUD MICROPHYSICS

Microphysics models used by the PSM are patterned after the warm-cloud microphysics models of Kessler.[13] Conservation differential equations for concentrations of cloud water (mist) and precipitation water are presented. An exponential hydrometeor size distribution function is assumed. This choice of size distribution allows the details of hydrometeor size to be integrated out of the conservation equations.

For the microphysics calculations I assume a steady state and consider spatial variation in the vertical only; only the updraft velocity from the kinematic circulation model is used. The conservation equations are integrated by a conventional numerical method (Runge–Kutta) to yield concentrations of cloud and precipitation water as a function of altitude.

For cold (ice) clouds, the method departs substantially from the one derived by Kessler. For ice hydrometeors I use a parameterization of particle growth devised by Koenig[14] and an exponential size distribution described by Sekhon and Srivastava.[15]

Warm Clouds

Warm-cloud microphysics apply at temperatures above 0°C. I assume the Marshall–Palmer water drop size distribution function,[16] where the number of drops per unit volume of air in the diameter range dD centered on D is given by

$$dN_D = N_o e^{-\lambda D}\, dD \tag{11}$$

and N_o is a constant. For microphysics calculations only, I take the settling speed of a drop of diameter D to be

$$V = -faD^b \tag{12}$$

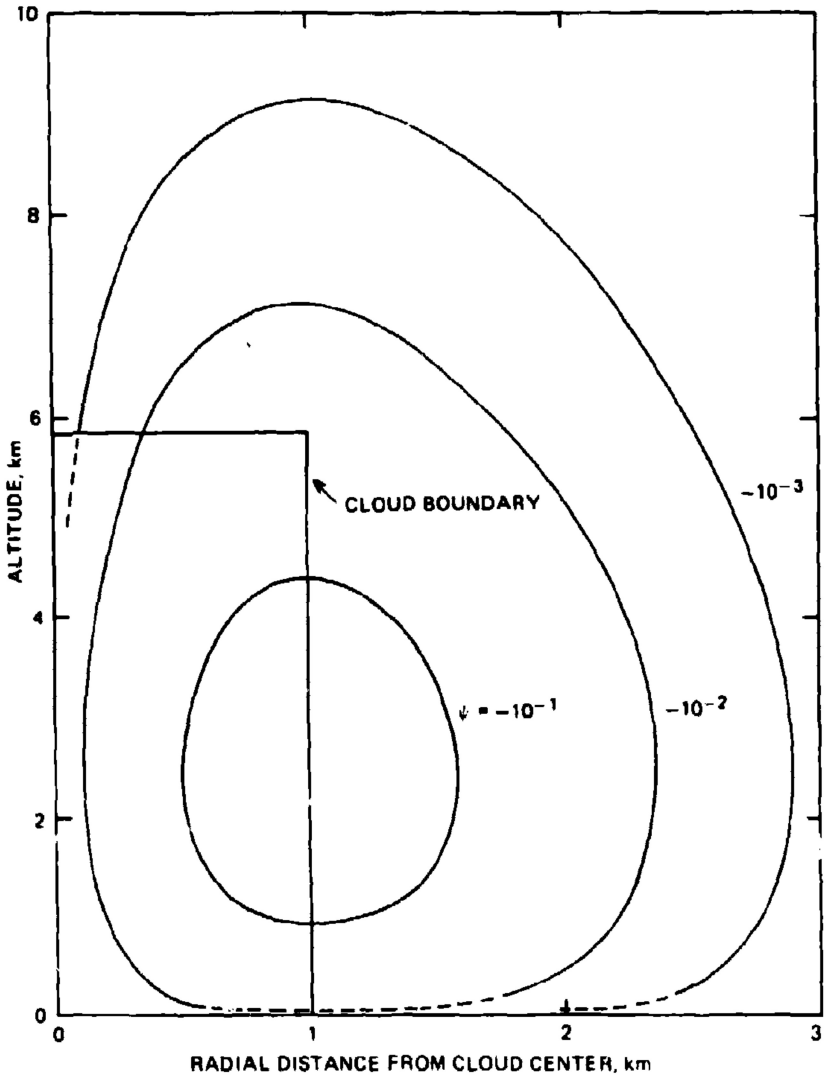

Fig. 1 Kinematic cumulus cloud circulation. Top is at 5.8 km, radius is 1 km. Maximum updraft flux is 13 kg m^{-2} sec^{-1}. (The ψ values should be multiplied by a constant factor of 13×10^6.)

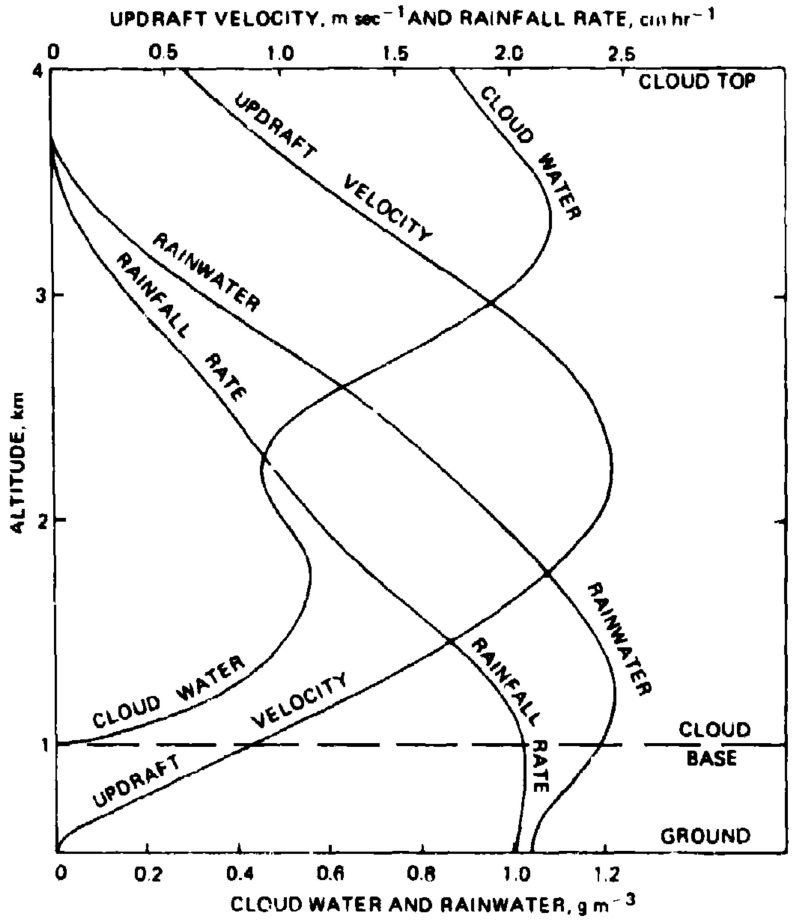

Fig. 2 Calculated microphysical structure for a storm cloud observed at Munich, Germany, on July 29, 1971. Rainfall at the ground and maximum updraft flux are assumed to be 20 mm hr $^{-1}$ and 6.5 kg m $^{-2}$ sec $^{-1}$, respectively. The ground is at 520 m and the cloud top at 4000 m altitudes.

From Eqs. 11 and 12 one can derive the relations

$$M = \frac{\pi \rho_w N_0}{\lambda^4} = \left(\frac{\phi}{\lambda}\right)^4 \tag{13}$$

and

$$\bar{V} = -f \frac{\Gamma(4+b)}{6} \frac{a}{\lambda^b} \tag{14}$$

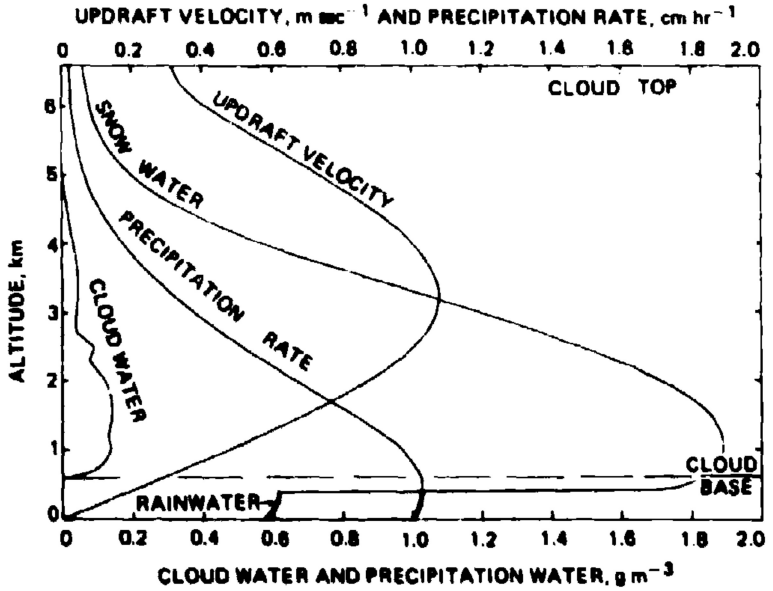

Fig. 3 Calculated microphysical structure for a storm cloud observed at Emden, Germany, on Feb. 3, 1969. Rainfall at the ground and maximum updraft flux are assumed to be 10 mm hr⁻¹ and 1.0 kg m⁻² sec⁻¹, respectively. The ground is at sea level and the cloud top at 6.6 km.

where $\bar{V}$ is a mass-weighted-average settling velocity.

We have two conservation equations: one for cloud water and one for precipitation water. In terms of the quantities above, these are

$$\frac{dm}{dz} = \frac{w\frac{m}{\rho}\frac{d\rho}{dz} + wG - k_K(m - a_K) - \frac{\pi}{4}a\Gamma(3+b)\,f\,\bar{E}\,N_0\left(\frac{M^{1/4}}{\phi}\right)^{3+b} m}{w} \tag{15}$$

and

$$\frac{dR_w}{dz} = k_K(m - a_K) + \frac{\pi}{4}a\Gamma(3+b)\,f\,\bar{E}\,N_0\left(\frac{M^{1/4}}{\phi}\right)^{3+b} m + 0.703 \times 10^{-4}(q - q_s)T\,[1 - 0.025(T - 290)] \times N_0\Gamma(2.615)\left(\frac{M^{1/4}}{\phi}\right)^{2.615} \tag{16}$$

Here R_w is vertical flux of precipitation water.

$$R_w = M(w + \bar{V}) \tag{17}$$

and G is the cloud water generating function

$$G = -\rho \frac{d(qs/\rho)}{dz} \tag{18}$$

In Eq. 15 the first term accounts for concentration change by expansion of a parcel of cloud as it rises, the second term accounts for condensation of water from the saturated air in the updraft, the third term is Kessler's parameterization of the conversion of cloud to precipitation by autocoalescence, and the final term accounts for loss of cloud to precipitation via inertial capture. In Eq. 16 the first two terms are equal but opposite in sign to the third and last terms in Eq. 15. These are applicable inside the cloud only. The last term applies only below the cloud in unsaturated air; it accounts for evaporation loss by use of an equation given by Nordquist.[17]

To obtain precipitation water concentration, M, from the flux, we combine Eqs. 13, 14, and 17 to obtain

$$R_w = M\left(w - f\frac{\Gamma(4+b)}{6}\frac{a}{\phi^b}M^{b-1}\right) \tag{19}$$

which is solved by second-order Newton-Raphson iteration.

Results of a warm cloud microphysics calculation are shown in Fig. 2 for the atmosphere data of Table 1. A cumulus-cloud structure is assumed.

Cold Clouds

At temperatures below 0°C, I assume an exponential snow size distribution function of the form described by Sekhon and Srivastava,[18]

$$dN_D = N_{0i}\, e^{-\lambda_i D}\, dD_i \tag{20}$$

This has a form similar to that for liquid water (Eq. 11); however, N_{0i} is a function of M_i, whereas N_{0i} is constant. Sekhon and Srivastava show that Eq. 20 and its algebraic derivatives can be made internally consistent and can represent observed data for a wide range of snow forms provided that

1. Size spectral data are normalized with respect to water content instead of particle number.
2. Distributions are corrected for truncation at their large particle tails.
3. Distribution parameters are based on empirical relations for settling speed and liquid-water content of the forms.

TABLE 1

ATMOSPHERE STRUCTURE FOR THE JULY 29, 1971, MUNICH STORM CLOUD*

Altitude, m	Pressure, mb	Temperature, °C	Relative humidity,† %
535	961	16.2	88
917	918	13.0	100
1157	892	11.8	100
1461	860	10.4	100(91)
1558	850	9.8	100(94)
1775	828	8.4	100
2362	771	7.2	100
3155	700	2.0	100
3364	682	0.6	100
4062	625	− 0.7	100
5809	500	−11.5	90
7125	420	−19.5	85
7489	400	−22.1	84
9540	300	−36.9	74
10799	250	−39.3	73

* Data obtained from Betty Jankus of Lawrence Livermore Laboratory.

† The two humidity values in parentheses actually were reported but were adjusted to 100% to avoid a discontinuity in the cloud.

$$V_i = -a_i D_i^{b_i} f_i \tag{21}$$

$$M_i = AR_i^B \tag{22}$$

where a_i, b_i, A, and B are constants.

By use of Eqs. 20, 21, and 22, one can derive the following expressions that are used in the conservation equations:

$$\lambda_i = \left[\frac{1}{6} a_i A^{1-B} C\Gamma(4 + b_i) f_i\right]^{1/b_i} M_i^{(1-B)/Bb_i} \tag{23}$$

$$N_{oi} = \frac{1.2285}{\pi \rho_w} \lambda_i^4 M_i \tag{24}$$

$$N_i = \frac{0.391 \lambda_i^3 M_i}{\rho_w} \tag{25}$$

$$V_i = -\frac{f_i}{A^{1-B} C} M_i^{(1-B)/B} \tag{26}$$

Here C is a factor, given by Sekhon and Srivastava, to correct for size spectrum truncation.

The conservation equation for snow water is taken to consist of terms representing the processes

$$\frac{dR_i}{dz} = (\text{nucleation} + \text{condensation growth}) + (\text{glaciation of cloud water}) + (\text{riming growth}) - (\text{evaporation})$$

The first three terms apply inside the cloud only, and the final term applies below the cloud only. Each term is discussed below.

Partition of condensing vapor between ice and cloud water and glaciation of cloud water are taken to be functions of temperature in this model. Although these processes, particularly the latter, may occur discontinuously in a growing cumulus cloud, such a mechanism is inapplicable in a steady-state cloud. In lieu of knowledge of the actual mechanisms involved, I have arbitrarily chosen simple, plausible models for these processes. Between $-5°$ and $-35°C$ water condensing from the vapor is partitioned between ice and liquid as a linear function of temperature. Below $-35°C$ all condensation is to the ice phase. The equation is

$$\left.\frac{dR_i}{dz}\right|_{\substack{\text{nucl.}\\+\\\text{cond}}} = -\,w\,G\,\max\left(\frac{T-268}{30}, -1\right) \quad (T < 268°K) \tag{27}$$

where the factor max(x,y) has a value that is the maximum of x and y. Glaciation is assumed to be an exponential function of temperature below $-5°C$, namely,

$$\left.\frac{dR_i}{dz}\right|_{\text{glac}} = -\,w\,\frac{m}{10}\,\frac{dT}{dz} \quad (238°K < T < 268°K) \tag{28}$$

At the altitude where $T = 238°K$, any cloud water still extant is converted to the ice phase.

Riming growth is computed by Koenig's parameterization.[14] Specifically, Koenig's growth regimes $B \rightarrow C$, $C \rightarrow D$, and $D \rightarrow \infty$ are used. Koenig's growth-median particle mass, m_g, is

$$m_g = \frac{15.016\,\alpha_i^3\,M_i}{\rho_w N_i} \quad \text{(in mks units)} \tag{29}$$

Here α_i is a constant defined by

$$\alpha_i = D_{10}\,\lambda_i \tag{30}$$

where D_{i0} is the volume-median diameter of the melted-drop diameter distribution. The value $\alpha_i = 3.2$ is used as recommended by Sekhon and Srivastava for a truncated distribution. (Note that liquid-water density, ρ_w, instead of ice density appears in Eq. 29 because of our use of melted-drop diameter.) In terms of Koenig's growth regimes, riming growth is

$$\left.\frac{dR_i}{dz}\right|_{rim.} = N_i \left.\frac{dm_s}{dt}\right|_{\substack{B \to C \\ C \to D \\ \text{or} \\ D \to *}} \tag{31}$$

The expression for evaporation of ice falling in unsaturated air is derived with the use of the equation for water drops given by Nordquist.[17] The expression is

$$\left.\frac{dR_i}{dz}\right|_{evap.} = 0.703 \times 10^{-4}\,\Gamma(2.615)(q - q_{si}) \times T[1 - 0.025(T - 290)]\, N_i \left(\frac{M_i}{\pi \rho_w N_i}\right)^{0.525} \tag{32}$$

Finally, take the sum of Eqs. 27, 28, 31, and 32,

$$\frac{dR_i}{dz} = \left.\frac{dR_i}{dz}\right|_{\substack{nucl. \\ + \\ cond.}} + \left.\frac{dR_i}{dz}\right|_{diff.} + \left.\frac{dR_i}{dz}\right|_{rim.} + \left.\frac{dR_i}{dz}\right|_{evap.} \tag{33}$$

For cloud water the conservation equation is

$$\frac{dm}{dz} = \frac{m}{\rho}\frac{d\rho}{dz} + G - \frac{\left.\frac{dR_i}{dz}\right|_{\substack{nucl. \\ + \\ cond.}} + \left.\frac{dR_i}{dz}\right|_{diff.} + \left.\frac{dR_i}{dz}\right|_{rim.}}{w} \quad (T < 238°K) \tag{34}$$

Snow concentration, M_i, is obtained from the flux by Newton–Raphson solution of the equation

$$R_i = M_i\left[w - \frac{f_i}{A^{1/B} C} M_i^{(1-B)/B}\right] \tag{35}$$

Both snow and liquid-water precipitation can exist in the same cloud though not at the same altitude. On passing through 0°C, precipitation water changes phase; cloud water does not. All ice-phase water is categorized as precipitation water.

Results of a cold cloud microphysics calculation are shown in Fig. 3 for the atmosphere data of Table 2. A stratus cloud structure is assumed.

AEROSOL SCAVENGING

Aerosol scavenging processes are separated into two main categories: (1) Below-cloud scavenging and (2) in-cloud scavenging. Below-cloud scavenging is by the relatively well understood and straightforward process of inertial capture by precipitation. In-cloud scavenging is by more complex multistage processes. The particular process used is selected by the code on the basis of debris particle properties and local conditions.

Scavenging mechanisms are limited to those considered fast enough to be of importance to tactical military operations. Thus phoretic scavenging,[18,19] electrical interaction, and small-scale turbulence effects are not included, although these processes probably are important over long spans of time.

Below-Cloud Scavenging

Below-cloud scavenging is an exponential function of time given by

$$M(t)_A = M(0)_A \exp(-\Lambda t) \tag{36}$$

where $M(0)_A$ is the initial aerosol concentration, $M(t)_A$ is unscavenged aerosol concentration after exposure to precipitation for time t, and Λ is the "washout coefficient."[20,21] The washout coefficient is given by

$$\Lambda = \frac{\pi}{4} \sum_D (D + \delta)^2 \, |V(D) - V(\delta)| \, E(D,\delta) \, N_D \tag{37}$$

In the PSM the hydrometeor size distribution is represented by discrete size classes, the number of class subdivisions being specified by input to the code. In Eq. 37 the summation is over the size classes, and D represents the central hydrometeor diameter of each class. For water drops V(D) is computed by the ninth-order polynomial approximation of Foote and duToit[22] with their altitude correction; Langmuir[23] collection efficiencies, $E(D,\delta)$, are used. For snow Eq. 21, with coefficients recommended by Langleben[24] for crystal aggregates, is used for V(D), and Ranz and Wong[25] collection efficiencies for disks are used. The value for $V(\delta)$ is computed by Davies' equations for spheres.[26] The value of N_D is computed by integration of Eq. 11 or Eq. 20 over each

TABLE 2

ATMOSPHERE STRUCTURE FOR THE FEB. 3, 1969, EMDEN STORM CLOUD

Altitude, m	Pressure, mb	Temperature, °C	Relative humidity,* %
7	993	1.8	97
155	975	0.2	97
460	938	0.0	100
676	912	− 2.1	100
818	895	− 2.5	100
1244	850	− 5.5	100
2737	700	−16.1	100
3250	658	−19.5	100
5179	500	−35.9	100
6251	411	−47.5	100
6687	400	−48.9	100
7155	375	−51.1	90
8559	300	−51.1	87
10169	239	−51.1	79

* Above 818 m the recorded humidity data were incomplete and erratic. Values of 100% were used up to the inversion at about 6600 m.

size class interval. Here and elsewhere atmospheric and microphysical data for the center point of the space cell being traversed are used in the calculations. Exposure time, t, is the cell transit time of the unscavenged debris parcel.

Computed rainout and snowout efficiencies are shown in Figs. 4 and 5.

In-Cloud Scavenging

In the PSM the most important in-cloud scavenging mechanism is as follows: Aerosol particles nucleate water drops or ice crystals which then grow by condensation from the vapor. As they grow the aerosol-containing hydrometeors are exposed to inertial capture by precipitation. This process (the NCI process) yields in-cloud scavenging rates that are fast enough to be in accord with observed data (e.g., see Ref. 27).

In the presence of high cloud water droplet concentrations, Brownian diffusion capture of submicron aerosol particles by the cloud droplets also may be important. Again the scavenging is by a multistep process: Diffusion capture of aerosol particles followed by inertial capture of the cloud droplets by precipitation. This process (the BCI process) also is included in the PSM.

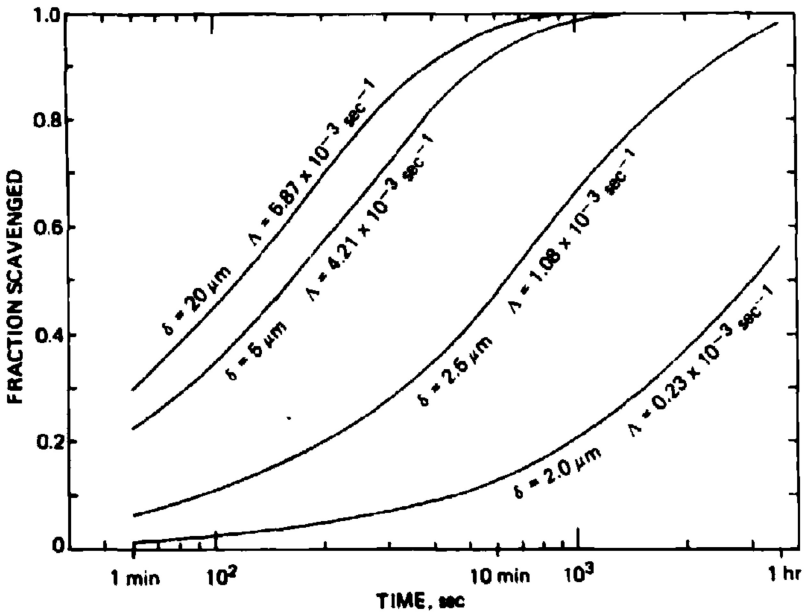

Fig. 4 Below-cloud (z = 881 m) rainout efficiency for the Munich July 29, 1971, cloud.

Although there is no theoretical limitation on the size of aerosol particles that can be scavenged by the BCI process (except, of course, the lower limit imposed by molecular dimensions), for practical purposes it is limited to very small particles in the presence of high concentrations of cloud droplets. On the other hand, the NCI process is profoundly restricted by a lower limit on the size of nucleating aerosol particle, the "critical nucleation" diameter, which is determined by local conditions in the cloud. Aerosol particles that are smaller than the critical size cannot nucleate water drops (or ice crystals) and therefore cannot be scavenged by the NCI process. Whenever the NCI process dominates in-cloud scavenging, which is the usual situation, this effectively imposes a lower size limit on the aerosol particles that can be scavenged.

Liquid-Phase Nucleation Followed by Condensation Growth

Nucleation and condensation-growth theory is treated in detail by Fletcher[28] and Squires.[29] If we assume that nuclear-debris particles are wettable but insoluble[30] and that ionization effects are negligible,[31] the condensation-growth equation is approximately

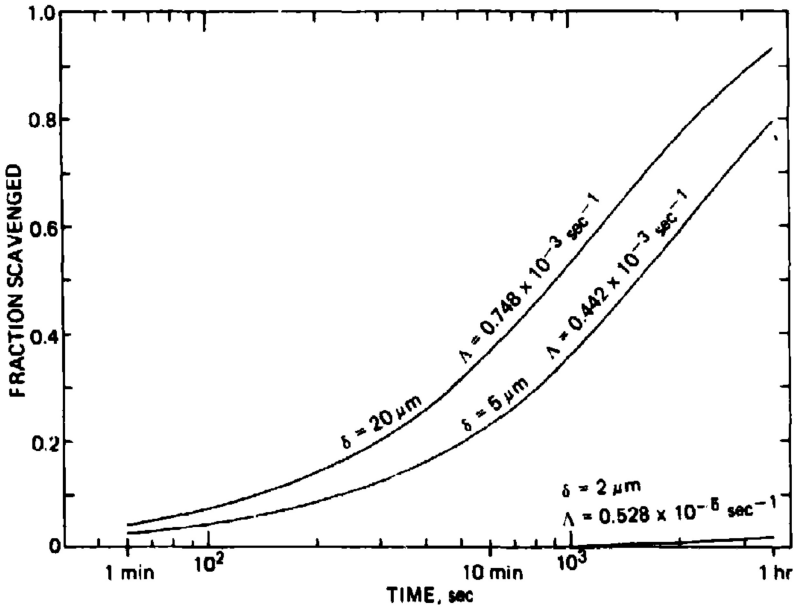

Fig. 5 Below-cloud (z = 438 m) snowout efficiency for the Emden Feb. 3, 1969, cloud.

$$\frac{d(\delta^3)}{dt} = 12QS(\delta - \delta^*)\, f_v \tag{38}$$

where

$$Q = \frac{K_v q_s/\rho_w}{[1 + (K_v L^2 q_s \epsilon/R_a T^2 \kappa)]} \tag{39}$$

$$S = \frac{P_v - P_{vs}}{P_{vs}} \tag{40}$$

$$\delta^* = \frac{4\sigma\epsilon}{\rho_w R_a T S} \tag{41}$$

For monodisperse particles with number concentration N in an updraft, w, the supersaturation rate of change is

$$\frac{dS}{dt} = \alpha w - \frac{1}{2}\beta_2 N S \delta \tag{42}$$

where

$$\alpha = \frac{g}{R_a T}\left(\frac{L\epsilon}{TC_p} - 1\right) \tag{43}$$

$$\beta_2 = 4\pi \frac{\rho_w}{\rho} Q\left(\frac{L^2\epsilon}{R_a T^2 C_p} + \frac{\rho}{q_s}\right) \tag{44}$$

In these equations δ represents initially the debris particle diameter and subsequently the diameter of the debris-containing water drop. Notice that the particle volume growth rate (Eq. 38) is positive only if $\delta > \delta^*$. The term δ^* is the critical nucleation diameter (Eq. 41), which is discussed near the end of the preceding section.

The first term on the right side of Eq. 42 represents an increase of S by adiabatic expansion cooling of air as it rises in the updraft, whereas the second term represents decay of S by condensation on the growing water drops. Since we begin with a steady-state cloud that is then perturbed by entering aerosol particles, we drop the first term and initiate solution of Eqs. 38 and 42 with a maximum S.

Twomey[32] shows that in normal cloud development S approaches a maximum given by

$$S_{max} = \left[\frac{(8\alpha^3)^{1/2} w^{3/2}}{\beta_1 ckB\left(\frac{k}{2}, \frac{3}{2}\right)}\right]^{1/(k+2)} \tag{45}$$

where

$$\beta_1 = (2Q)^{1/2}\beta_2 \tag{46}$$

provided that the number of active condensation nuclei (per unit volume of air), N(S), at supersaturation S is

$$N(S) = cS^k \tag{47}$$

For nonprecipitating continental clouds, Twomey suggests

$$c = 6 \times 10^9 \ (m^{-3})$$

$$k = 0.4$$

These values were used in the calculations reported here.

Initially S apparently lies between S_{max} and 0; however, I have no way to determine the appropriate value. The major effect of decreasing

$S_{initial}$ below S_{max} is to increase δ^* proportionately (see Eq. 41). To be conservative (overestimation of scavenging is preferred), I have used $S_{initial} = S_{max}$ in the calculations reported here.

In summary, water condensation growth on debris particles is computed (see Fig. 6) by numerical integration of the coupled equations

$$\frac{d(\delta^3)}{dt} = 12QS(\delta - \delta^*)\, f_v \tag{38}$$

$$\frac{dS}{dt} = -\frac{\beta_2 N_\delta S\delta}{2} \tag{48}$$

starting with $S_{initial} = S_{max}$ and $\delta_{initial}$ = debris particle diameter. The term f_v is given a constant value of 1.15. The various other parameters are computed from local conditions in the cloud, and the integration is over the exposure time interval.

Ice-Phase Nucleation Followed by Condensation and Riming Growth

This process is similar to that described in the preceding section; however, it is intrinsically much more difficult because one must deal with crystalline water. Fortunately most of the complexities can be avoided by use of the parameterized ice-growth equations developed by Koenig.[14]

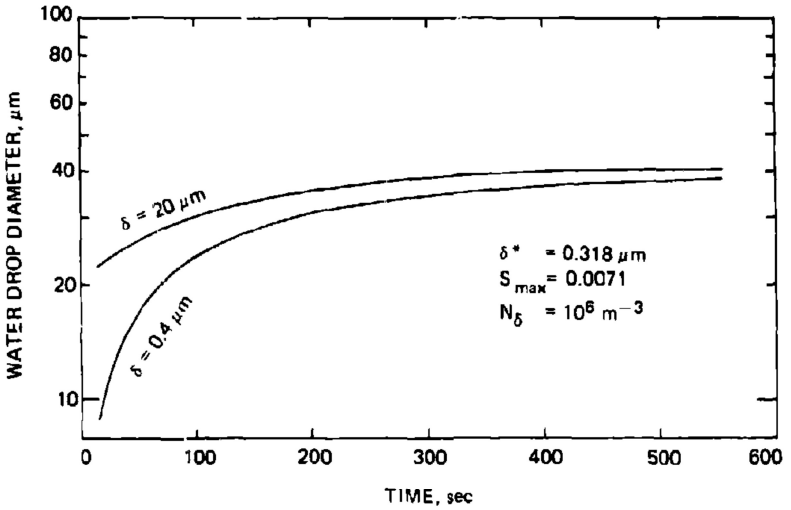

Fig. 5 Condensation growth of fallout-containing water drops computed at z = 1409 m in the Munich July 29, 1971, cloud.

Under steady-state conditions nucleation of ice crystals proceeds by the sublimation mechanism (i.e., vapor → ice without involvement of the liquid phase).[28,33] As with liquid-phase nucleation, there exists a critical nucleation diameter, δ_i^*, below which condensation growth cannot be sustained. If we neglect deviations from spherical shape, neglect elastic strain at the ice-particle interface, and assume that the angle of contact between ice and particle surfaces is zero, we have

$$\delta_i^* \simeq \frac{4\sigma_{vi}\epsilon}{\rho_i R_a T \ell n \frac{P_v}{P_{vsi}}} \tag{49}$$

This equation yields a conservative estimate of δ_i^* in the sense that inclusion of effects of elastic strain and nonzero contact angle will increase δ_i^*.

Since we expect some liquid water to be present in the cloud except at extremely cold temperatures (−35°C and below), P_v can be replaced by P_{vs} in Eq. 49. Since $\ell n\,(P_{vs}/P_{vsi})$ is a function of temperature (see Appendix 2), δ_i^* is a function of temperature. Representative values of δ_i^* computed from Eq. 49 are

Temperature, °C	δ_i^*, μm
− 5	0.095
−10	0.048
−20	0.025

If a fallout particle diameter is larger than the critical value, it is allowed to grow by condensation and/or riming according to Koenig's parameterized equations.[14] If m_i is the mass of the ice crystal, then

$$\frac{dm_i}{dt} = a_1 m_i^{a_2} \tag{50}$$

where a_1 and a_2 are tabulated by Koenig as functions of temperature for condensation growth and temperature and cloud water concentration for riming growth. Equation 50 is integrated over the exposure time interval to yield the particle growth (see Fig. 7). As usual, equation parameters are evaluated for local conditions in the cloud.

Time-Dependent Inertial Capture

A growing hydrometeor–particle combination (HPC) is subject to inertial capture by precipitation. Since the HPC properties are a function

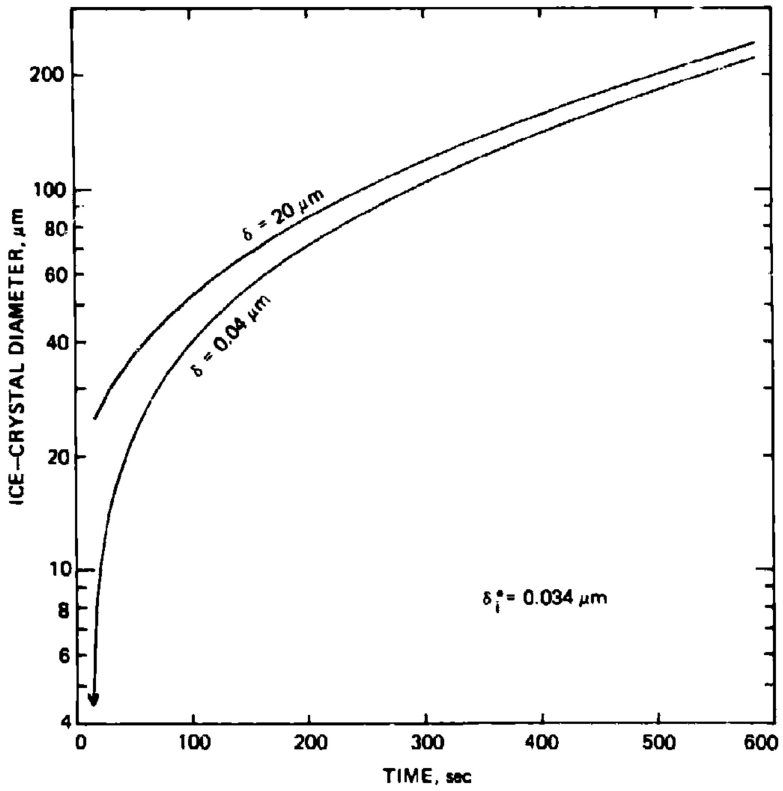

Fig. 7 Condensation and riming growth of fallout-containing ice crystals computed at z = 2494 m in the Emden Feb. 3, 1969, cloud.

of time, the washout coefficient (Eq. 37) becomes a function of time. Therefore the scavenging rate equation is

$$\frac{dM(t)_\delta}{dt} = -\Lambda(t)\, M(t)_a \tag{51}$$

which integrates to

$$M(t)_\delta = M(0)_\delta \exp\left[-\int_0^t \Lambda(\xi)\, d\xi\right] \tag{52}$$

In the process of calculating HPC growth by one of the procedures described in the preceding two sections, the PSM stores a table of HPC

diameters and densities as a function of time. A corresponding washout coefficient is computed for each table entry, and the integral in Eq. 52 is then calculated by Gaussian quadrature of the tabulated Λ values.

Brownian Diffusion Scavenging

Very small particles possess little inertia relative to the random molecular motion of their carrier gas. Consequently they are subject to Brownian diffusive transport in the gas and will impact on and coalesce with larger water drops. The theory is reviewed by Slinn and Hales[18] and Fuchs.[34] After a particle is collected by a cloud droplet, the particle-droplet combination (DPC) is subjected to inertial capture by precipitation.

The rate of change of aerosol concentration via Brownian capture is

$$\frac{dN_\delta}{dt} = -\pi K D N_\delta N_D S_h \tag{53}$$

where the Brownian diffusion coefficient for the collected particles, K, is

$$K = \frac{RT}{3\pi\gamma A_n \delta}\left(1 + \frac{2\nu}{\delta}\right) \tag{54}$$

and

$$\nu = 0.9\gamma\left(\frac{\pi}{2P\rho}\right)^{1/2} \tag{55}$$

For steady-state cloud conditions, this is integrated to yield an exponential scavenging rate

$$N(t)_\delta = N(0)_\delta\left(\exp - \frac{t}{\tau}\right) \tag{56}$$

with time constant, τ, given by

$$\tau = \frac{1}{\pi K D N_D S_h} \tag{57}$$

On the basis of data summarized by Mason,[35] I take D = 10 μm for stratus cloud and D = 40 μm for cumulus cloud. The value of N_D is computed from m with the use of one of these droplet diameters.

Define $\lambda_B = 1/\tau$ and let Λ be the washout coefficient for the DPC. At exposure time t define $M(t)_a$, the concentration of unscavenged aerosol; $M(t)_{a|c}$, the concentration of aerosol associated with cloud droplets; and $M(t)_{a|P}$, the concentration of aerosol associated with precipitation. Then the rate equations are

$$\frac{dM(t)_a}{dt} = -\lambda_B M(t)_a \tag{58}$$

$$\frac{dM(t)_{a|c}}{dt} = \lambda_B M(t)_a - \Lambda M(t)_{a|c} \tag{59}$$

$$\frac{dM(t)_{a|P}}{dt} = \Lambda M(t)_{a|c} \tag{60}$$

and these can be integrated to yield

$$\frac{M(t)_a}{M(0)_a} = e^{-\lambda_B t} \tag{56'}$$

$$\frac{M(t)_{a|c}}{M(0)_a} = \frac{\lambda_B}{\Lambda - \lambda_B}\left(e^{-\lambda_B t} - e^{-\Lambda t}\right) \tag{61}$$

$$\frac{M(t)_{a|P}}{M(0)_a} = \frac{\Lambda\lambda_B}{\Lambda - \lambda_B}\left[\frac{1}{\Lambda}\left(e^{-\Lambda t} - 1\right) - \frac{1}{\lambda_B}\left(e^{-\lambda_B t} - 1\right)\right] \tag{62}$$

Equation 62 is used to compute Brownian scavenging in the PSM.

In-Cloud Scavenging Results

Figures 8 to 11 show in-cloud scavenging efficiency results for the Munich and Emden clouds. "Nominal" washout coefficients, (Λ), are computed from the equation

$$(\Lambda) = -\frac{\ell n(1 - f_{sca})}{t}$$

where f_{sca} is the fraction scavenged as shown in Figs. 8 and 10.

To the right of the critical nucleation diameter discontinuities, scavenging is by the NCI process; to the left it is by the BCI process. If slower scavenging mechanisms, such as phoresis and autocoalescence, were included, the depth and steepness of the discontinuities would probably be moderated.

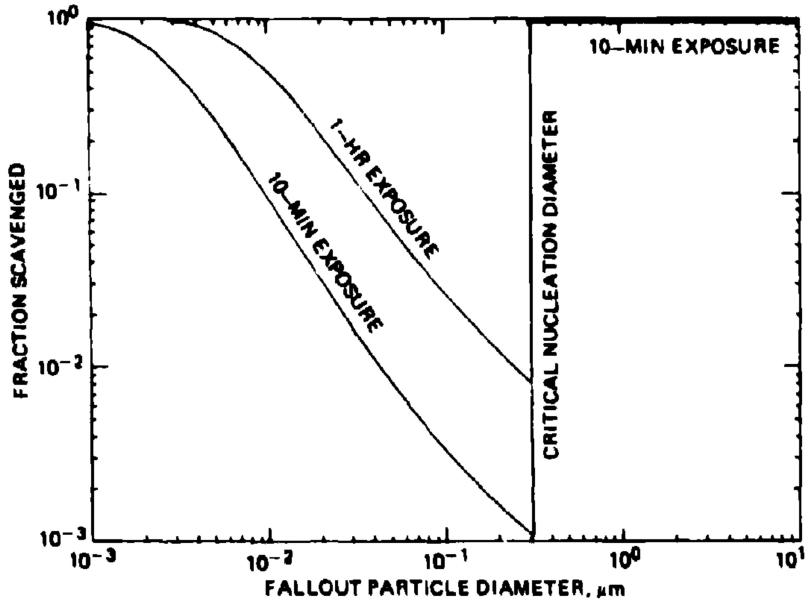

Fig. 8 Scavenging efficiency at z = 1409 m in the Munich July 29, 1971, cloud.

Distribution of Scavenged Aerosol over the Hydrometeor Size Spectrum

The final step in each of the scavenging mechanisms is inertial collection by precipitation. The basic assumption here is that scavenged aerosol is distributed across the hydrometeor size spectrum in proportion to scavenging rate across the hydrometeor size spectrum.

$$\frac{dM_A}{dt} = -\Lambda M_A \tag{63}$$

and the rate of scavenging by hydrometeors in the size class centered on D is

$$\left.\frac{dM_\delta}{dt}\right|_D = \frac{\pi}{4}(D+\delta)^2|V(D) - V(\delta)|E(D,\delta)\,N_D M_\delta = \Lambda_D M_A \tag{64}$$

Thus, for steady Λ the fraction of scavenged nuclear debris in the hydrometeor size class centered on D is

$$\Omega(D)_\delta = \frac{\Lambda_D}{\Lambda} \tag{65}$$

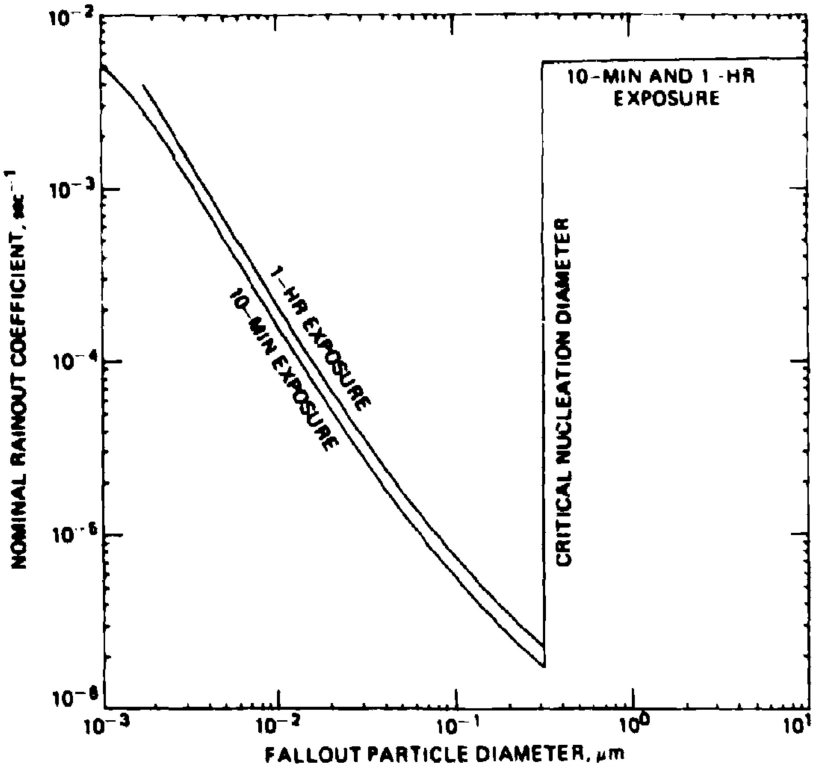

Fig. 9 Nominal rainout coefficients (see text) computed at z = 1409 m in the Munich July 29, 1971, cloud.

and for time-dependent Λ the result is

$$\Omega(D)_h = \frac{\int \Lambda(t)_D \, dt}{\int \Lambda(t) \, dt} \tag{66}$$

Representative results are shown in Figs. 12 and 13.

TRANSPORT OF SCAVENGED AEROSOL

After a nuclear debris parcel enters a storm-cloud space cell, it is transported across the cell (or cells) until a cell vertical boundary is encountered, and then the cell transit time is stored. With the use of the transit time as the exposure time, a fraction of the parcel is scavenged and then distributed over the precipitation hydrometeor size distribution.

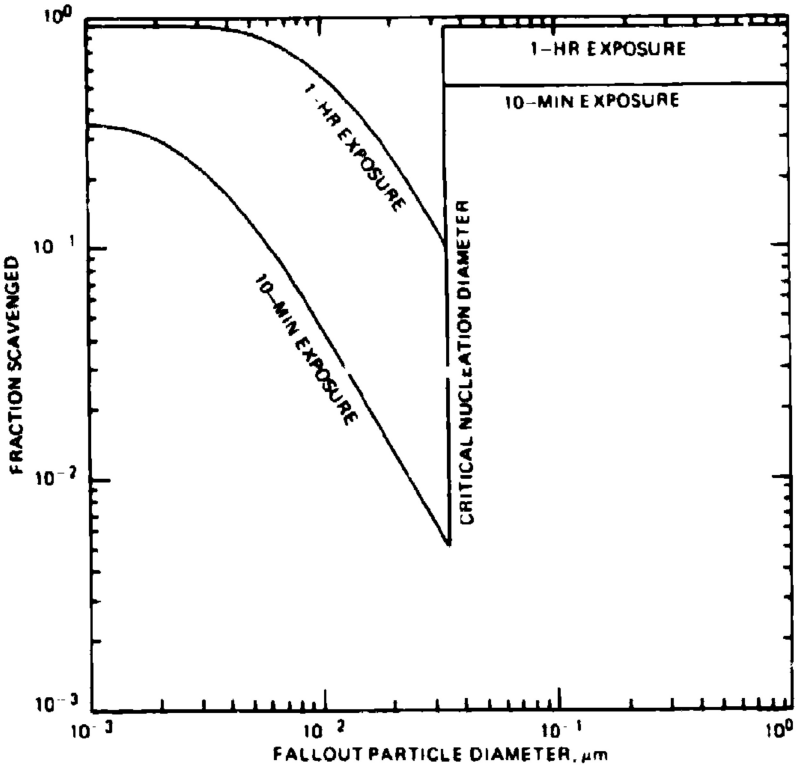

Fig. 10 Scavenging efficiency computed at z = 2494 m in the Emden Feb. 3, 1969, cloud.

Provided that the scavenged and distributed amounts of debris exceed threshold values, the hydrometeor-particle combinations (HPC) are transported to impact on the ground for each hydrometeor size class. Thus interaction of wind, including shear, with the different settling speeds across the HPC size spectrum (see Figs. 12 and 13) is accounted for in dispersing the material on the ground.[36]

The HPC transport is started at the center of the storm-cloud cell (or cells) in which the scavenging occurred. The HPC densities and diameters are adjusted to account for inclusion of the debris particle. This adjustment includes a correction for more than one particle per hydrometeor in case this should occur. Settling speeds for water drops[28] or snow aggregates,[15,24] corrected for altitude and HPC density, are used.

During transport to the ground, the HPC properties are kept constant except for phase change in passing through 0°C. No attempt is

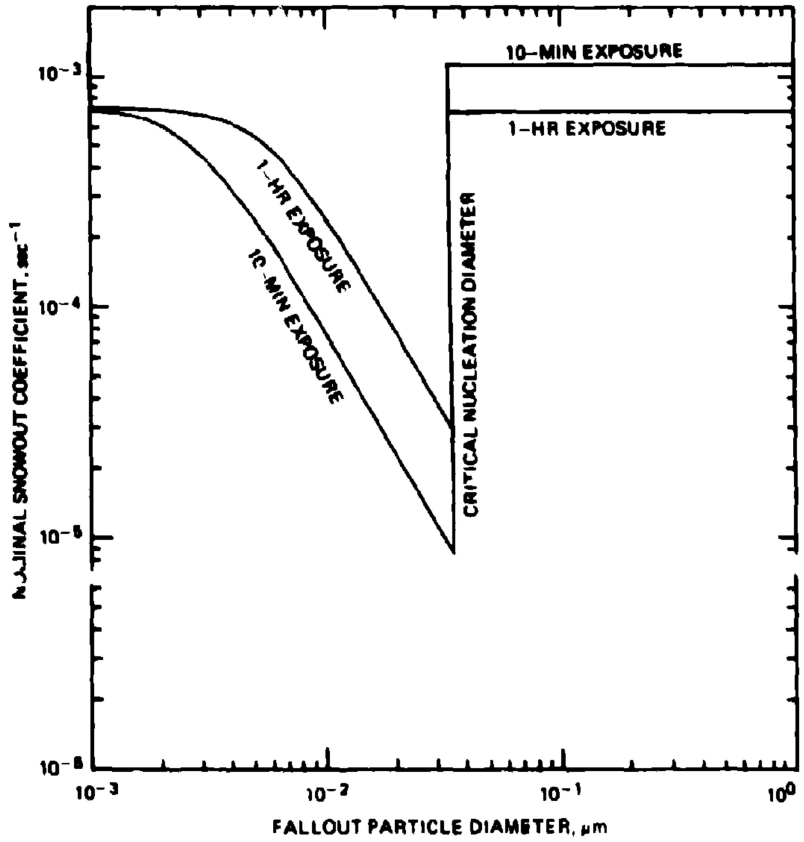

Fig. 11 Nominal snowout coefficients (see text) computed at z = 2494 m in the Emden Feb. 3, 1969, cloud.

made to account for redistribution of the debris owing to coalescence with cloud or with other precipitation. Evaporation in unsaturated air also is ignored. Error introduced is not known, but the coalescence and evaporation errors must be partly compensating.

RESULTS

A complete DELFIC-PSM calculation was done for a 0.05-kT airburst and the Munich storm of July 29, 1971 (see Fig. 2 and Table 1).

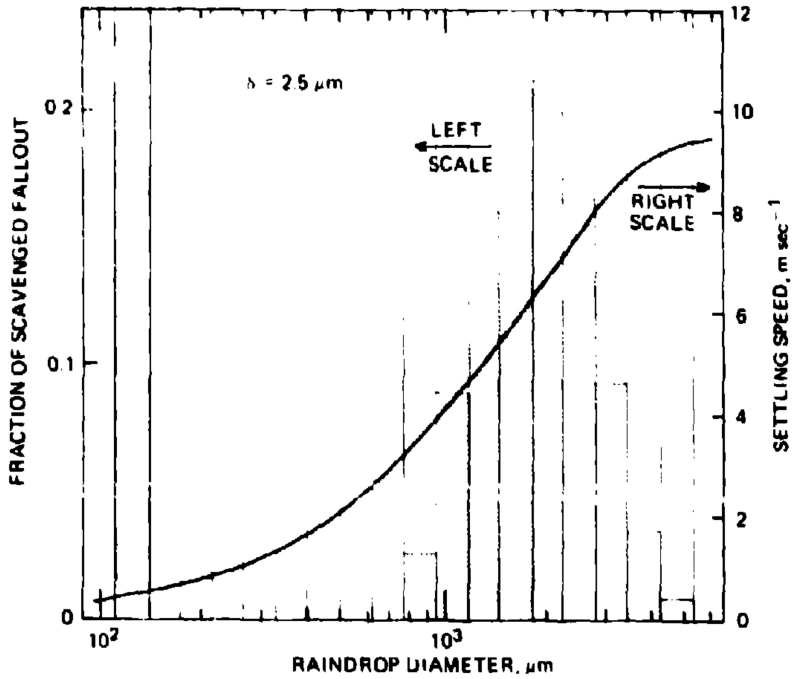

Fig. 12 Distribution of scavenged 2.5-μm-diameter particles over the raindrop spectrum computed below the Munich July 29, 1971, cloud at 881 m altitude.

Wind and turbulence data are given in Table 3. The nuclear explosion characteristics are

Energy yield (total and fission), kT	0.05
Ground altitude,* m	520
Height of burst above ground,† m	22.85
Cloud stabilization time, sec	610
Cloud top altitude, m	2424
Cloud base altitude, m	2153
Cloud radius, m	549

Cloud center was 4135 m east and 2387 m south of ground zero (GZ) at stabilization time

* All altitudes are relative to mean sea level.

† Chosen such that the nuclear fireball barely misses intersection with the ground.

A log-normal particle size distribution was used with a number distribution median diameter of 0.15 μm (volume median diameter 0.63 μm) and geometric standard deviation of 2.0 (Ref. 37). Fallout particle density is 5500 kg m $^{-3}$ (Ref. 37).

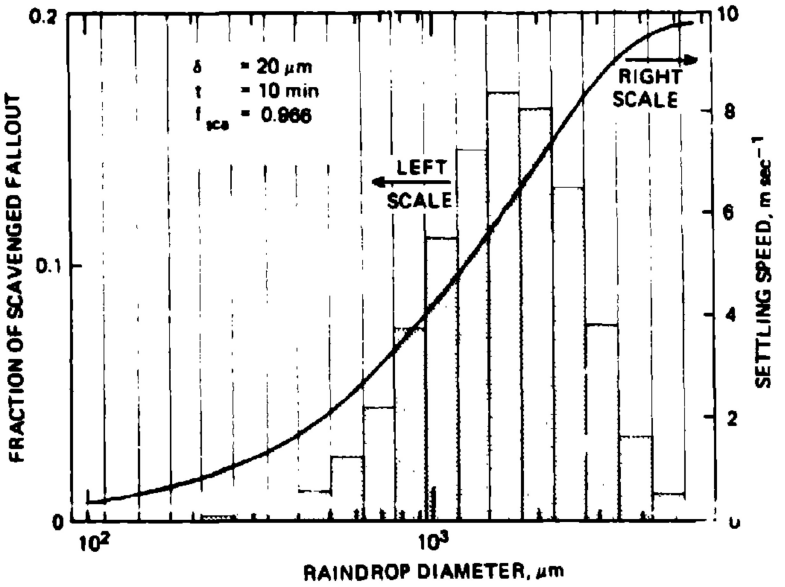

Fig. 13 Distribution of scavenged 20-μm-diameter particles over the raindrop spectrum computed in the Munich July 29, 1971, cloud at 1409 m altitude.

The storm, with a radius of 1.5 km, was centered 6 km east and 3 km south of GZ. Its position and characteristics were kept constant (tempor . change can be accommodated by the code).

The wet deposition fallout pattern is shown in Fig. 14. This map shows exposure rate [roentgens (R)/per hour] at 1 hr after detonation. It assumes complete deposition at 1 hr. About 18% of the total activity is deposited. The fallout is relatively widely dispersed on the ground, and, in terms of effects on military operations, radiation levels are not dangerously high. Somewhat less area dispersal and higher radiation intensities undoubtedly would be obtained if in-cloud downdraft regions were included in the modeling; however, this is offset by taking the cloud to be stationary.

Calculations also were attempted for explosions of 0.1 and 1.0 kT yield. The 0.1-kT nuclear cloud, with base at 2731 m, was too high to interact effectively with the storm cloud. The 1-kT nuclear cloud stabilized in the inversion above the storm-cloud top.

Intermediate scavenging results for the Munich rain cloud and a cold storm observed at Emden on Feb. 3, 1969 (see Fig. 3 and Table 2), are presented in Figs. 4 to 13. Figures 4 and 5 indicate a particle diameter

TABLE 3

WIND AND TURBULENCE DATA FOR MUNICH, JULY 29, 1971

Altitude, m	Wind velocity components,* m sec^{-1}		Turbulent energy dissipation rate, m^2 sec^{-3}
	East	North	
623	3.13	−1.81	1.00×10^{-4}
882	3.34	−1.93	3.00×10^{-4}
1173	3.57	−2.06	3.02×10^{-4}
1409	3.76	−2.17	3.03×10^{-4}
1588	3.90	−2.25	3.04×10^{-4}
1868	4.69	−1.27	4.00×10^{-4}
2414	4.16	−0.63	4.00×10^{-4}
3079	3.52	0.15	4.00×10^{-4}
3800	1.21	2.70	2.40×10^{-4}
4568	0.98	2.78	2.07×10^{-4}
5701	−0.10	4.54	1.58×10^{-4}
6887	−0.52	5.64	2.00×10^{-5}
7911	0.84	9.79	2.00×10^{-5}
9342	2.95	15.4	1.13×10^{-5}
10547	2.14	16.4	1.08×10^{-5}

* Wind data were obtained from Betty Jankus of Lawrence Livermore Laboratory. They do not include the kinematic storm-cloud contributions.

lower threshold for below-cloud scavenging of ~1.5 μm for both rain and snow.* Inside the rain cloud the critical nucleation diameter is about 0.3 μm, which effectively exempts smaller particles from scavenging (see Figs. 8 and 9).† For the snow cloud critical nucleation diameter is about an order of magnitude less (see Figs. 10 and 11). From consideration of Figs. 2 and 3, it is clear why nuclear debris entrained above the mid-altitude level of these clouds is not thoroughly scavenged: when the debris is entrained into the upper cloud, it is lifted into the cloud region that contains relatively little cloud and precipitation water.

SUMMARY

A single modular code has been developed that models the complete range of phenomenology pertinent to generation, transport, precipitation

* No below-cloud scavenging occurred in the complete calculation discussed above.

† For the particle size distribution used in the complete calculation and with uniform distribution of activity throughout particle volume, this exempts ~15% of the total activity from scavenging.

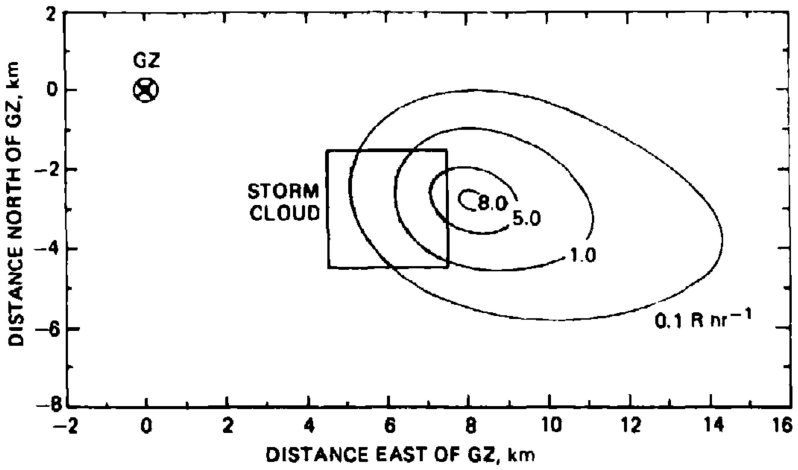

Fig. 14 Wet-deposition fallout map for a 0.05-kT airburst near the Munich July 29, 1971, storm. Exposure rate contours (R hr^{-1} at H + 1 hr) assume complete deposition at 1 hr after detonation.

scavenging, and deposition of wet and/or dry nuclear fallout. It is designed to study the significance of precipitation scavenging of nuclear debris to tactical military operations.

Intermediate calculated results are in accord with known cloud physics and scavenging data.

ACKNOWLEDGMENT

This work was sponsored by the Tactical Nuclear Division, Defense Nuclear Agency, Washington, D.C.

APPENDIX 1: SYMBOLS

a	Constant in the raindrop settling velocity approximation equation (Eq. 12) (a = 842).
a_l	Constant in the snow particle settling velocity equation (Eq. 21) (a_l = 8.629).
a_K	Kessler's autoconversion parameterization threshold (a_K = 0.0005) (kg m^{-3}).
A	Constant in Eq. 22 (A = 0.286).
A_n	Avogadro's number ($A_n = 6.023 \times 10^{23}$ $mole^{-1}$).
b	Constant in the raindrop settling velocity approximation equation (Eq. 12) (b = 0.8).

b_l	Constant in the snow particle settling velocity equation (Eq. 21) ($b_l = 0.31$).
B	Constant in Eq. 22 ($B = 0.86$).
B(x,y)	Complete beta function of arguments x,y.
c	Constant in Eq. 47 ($c = 6 \times 10^9$ m^{-3}).
C	Correction factor given by Sekhon and Srivastava[15] for snow particle size distribution truncation ($C = 0.86$).
C_P	Specific heat of air (joules kg^{-1} °K^{-1}) (see Appendix 2).
d	Differential operator.
D	Raindrop diameter (m).
D_l	Diameter of a melted snow particle (m).
$\overline{E}$	Average collection efficiency of cloud water by rain ($\overline{E} = 1$).
E(D,δ)	Efficiency of capture of aerosol particles of diameter δ by hydrometeors of diameter D.
f	Altitude correction factor for raindrop settling speed.[22]
f_{sca}	Fraction scavenged of an aerosol parcel.
f_l	Altitude correction factor for snow settling velocity.
f_v	Ventilation factor for growth of water drops ($f_v = 1.15$).
g	Gravity acceleration constant ($g = 9.8$ m sec^{-2}).
G	Cloud water generating function (Eq. 18) (kg m^{-4}).
k	Constant in Eq. 47 ($k = 0.4$).
k_K	Kessler's autoconversion parameterization constant ($k_K = 0.001$) (sec^{-1}).
K	Brownian diffusivity for small particles in air (m^2 sec^{-1}).
K_v	Diffusivity of water vapor in air (m^2 sec^{-1}) (see Appendix 2).
L	Latent heat of vaporization of water (joules kg^{-1}) (see Appendix 2).
m	Cloud water concentration (kg m^{-3}).
m_g	Koenig's growth-median ice particle mass (kg).
m_l	Mass of ice crystal (kg).
M	Rainwater concentration (kg m^{-3}).
M_l	Snow-water concentration (kg m^{-3}).
M_δ	Concentration of unscavenged aerosol of diameter δ (kg m^{-3}).
N_D	Number concentration of hydrometeors in the size class centered on D (m^{-3}).
N_{D_l}	Number concentration of snow particles in the size class centered on D_l (m^{-3}).
N_l	Total number concentration of snow particles (m^{-3}).
N_0	Constant in the Marshall–Palmer raindrop size distribution function ($N_0 = 8 \times 10^6$ m^{-4}).
N_{0l}	Parameter in the snow particle size distribution function (Eqs. 20 and 24) (m^{-4}).

N_δ	Number concentration of aerosol particles of diameter δ (m^{-3}).
P	Atmospheric pressure (Newtons m^{-2}).
P_v	Water-vapor pressure (Newtons m^{-2}).
P_{vs}	Saturation water-vapor pressure over water (Newtons m^{-2}).
P_{vsl}	Saturation water-vapor pressure over ice (Newtons m^{-2}).
q	Water-vapor density (kg m^{-3}).
q_s	Saturation water-vapor density over water (kg m^{-3}).
q_{sl}	Saturation water-vapor density over ice (kg m^{-3}).
Q	See Eq. 39.
r	Radial coordinate in an axially symmetric coordinate system (m).
R	Molar gas constant (R = 8.314 joules $°K^{-1}$ $mole^{-1}$).
R_a	Gas constant for air (R_a = 287.04 joules kg^{-1} $°K^{-1}$).
R_e	Reynolds number [$R_e = \rho DV(D)/\gamma$].
R_g	Precipitation flux at the ground (mm hr^{-1}).
R_i	Vertical flux of snow (kg m^{-2} sec^{-1}).
R_w	Vertical flux of rain (kg m^{-2} sec^{-1}).
S	Supersaturation of water vapor (Eq. 40).
S_c	Schmidt number [$S_c = \gamma/(\rho K)$].
S_h	Sherwood number [$S_h = 2(1 + 0.276\ R_e^{1/2}\ S_c^{1/3})$].
t	Time (sec).
T	Temperature (°K).
U	Radial velocity component in an axially symmetric flow (m sec^{-1}).
V	Raindrop gravity settling velocity (m sec^{-1}).
$\bar{V}$	Mass-weighted-mean water-drop settling velocity (Eq. 14) (m sec^{-1}).
V_i	Snow particle gravity settling velocity (Eq. 21) (m sec^{-1}).
$\bar{V}_i$	Mass-weighted-mean settling velocity for snow particles (Eq. 26) (m sec^{-1}).
V(D)	Settling speed of hydrometeor of diameter D (m sec^{-1}).
$V(\delta)$	Settling speed of aerosol particle of diameter δ (m sec^{-1}).
w	Vertical component of air velocity (m sec^{-1}).
z	Vertical coordinate (m).
α	See Eq. 43.
α_i	See Eq. 30.
β_1	See Eq. 46.
β_2	See Eq. 44.
γ	Dynamic viscosity of air (kg m^{-1} sec^{-1}).
$\Gamma(x)$	Gamma function of argument x.
δ	Aerosol particle diameter (m).

δ^* Critical nucleation diameter for condensation growth of water drops (Eq. 41) (m).
δ_i^* Critical nucleation diameter for condensation growth of ice particles (Eq. 49) (m).
ϵ Molecular weight ratio of water to air ($\epsilon = 18/29$).
ζ Nondimensional pressure in the storm cloud (Eq. 5).
η Nondimensional radial coordinate (Eq. 6).
κ Thermal conductivity of air (joules m^{-1} sec^{-1} $°K^{-1}$) (see Appendix 2).
λ Parameter in the Marshall–Palmer raindrop size distribution function (Eqs. 11 and 13) (m^{-1}).
λ_B Inverse of diffusive capture time constant ($\lambda_B = 1/\tau$) (sec^{-1}).
λ_i Parameter in the snow size distribution function (Eqs. 20 and 23) (m^{-1}).
Λ Inertial capture washout coefficient (Eq. 37) (sec^{-1}).
Λ_D Inertial capture washout coefficient for hydrometeors in the size class centered on D (sec^{-1}).
ν 0.9 × (mean free path of air) (Eq. 55) (m).
ρ Air density (kg m^{-3}).
ρ_i Density of ice particles (kg m^{-3}).
ρ_w Liquid-water density (kg m^{-3}).
σ Surface tension of water (Newtons m^{-1}).
σ_{vi} Free energy per unit area of ice-vapor interface ($\sigma_{vi} = 0.1$ joule m^{-2}).[28]
τ Diffusive capture time constant (Eqs. 56 and 57) (sec).
ϕ See Eq. 13.
Φ Storm-cloud radius (m).
ψ Stream function for storm-cloud circulation (kg m^{-2} sec^{-1}).
$\Omega(D)_\delta$ Fraction of scavenged aerosol of diameter δ in the hydrometeor size class centered on D.

APPENDIX 2: APPROXIMATION EQUATIONS FOR PHYSICAL PARAMETERS

Specific heat of air at constant pressure

$$C_p = 946.6 + 0.1971\ T \quad \text{(joules kg}^{-1}\ °K^{-1}\text{)}$$

Diffusivity of water vapor in air

$$K_v = \frac{2.26}{P}\left(\frac{T}{273}\right)^{1.81} \quad (m^2\ sec^{-1})$$

Latent heat of vaporization of water

$$L = 3.1603 \times 10^{6} - 2407.4\,T \quad \text{(joules kg}^{-1}\text{)}$$

Saturation water-vapor density over water

$$q_s = \frac{611\epsilon}{R_v T}\left(\frac{273}{T}\right)^{5.13} \exp\left[\frac{25(T-273)}{T}\right] \quad \text{(kg m}^{-3}\text{)}$$

Saturation water-vapor density over ice

$$q_{si} = \frac{1.32059}{T}\left(\frac{T}{273}\right)^{3.36854} \exp\left[-\frac{0.007391}{T}(T-2834)(T-273)\right] \quad \text{(kg m}^{-3}\text{)}$$

Thermal conductivity of air

$$\kappa = \left(\frac{9.5435}{T+120}\right)\left(\frac{T}{273}\right)^{3/2} \quad \text{(joules m}^{-1}\text{ sec}^{-1}\,^{\circ}\text{K}^{-1}\text{)}$$

Surface tension of water

$$\sigma = 0.0757 - 1.535 \times 10^{-4}(T-273) \text{ (Newtons m}^{-1}\text{)}$$

Saturation vapor-pressure ratio

$$\ln\left(\frac{P_{vs}}{P_{vsi}}\right) = 0.00970\,(273 - T)$$

REFERENCES

1. H. G. Norment, W. Y. G. Ing, and J. Zuckerman, Department of Defense Land Fallout Prediction System. Vol. II. Initial Conditions, Report DASA-1800-2 (AD-803144L), Technical Operations, Inc., Sept. 30, 1966; H. G. Norment, Report DNA-1800-2 (Suppl.) (AD-753842), Mt. Auburn Research Associates, October 1972.
2. H. G. Norment and S. Woolf, Department of Defense Land Fallout Prediction System Vol. III (Rev.), Report DASA-1800-3 (Rev.) (AD-879890L), Arcon Corporation, Sept. 1, 1970.
3. H. G. Norment and E. J. Tichovolsky, A New Fallout Transport Code for the DELFIC System: The Diffusive Transport Module, Report DASA-2669 (AD-727613), Arcon Corporation, Mar. 1, 1971; H. G. Norment, Report DNA-2669 (Suppl.) (AD-751542), Mt. Auburn Research Associates, October 1972.
4. R. C. Tompkins, Department of Defense Land Fallout Prediction System. Vol. V. Particle Activity, Report DASA-1800-5 (NDL-TR-102, AD-832239L), February 1968.

5. H. G. Norment, A Revised Output Processor Module for the DELFIC Fallout Prediction System, Report DNA-2962F (AD-751543), Mt. Auburn Research Associates Inc., October 1972.
6. I. O. Huebsch, The Development of a Water-Surface-Burst Fallout Model: The Rise and Expansion of the Atomic Cloud, Report USNRDL-TR-741 (AD-441983), Naval Radiological Defense Laboratory, Apr. 23, 1964; I. O. Huebsch, The Formation, Dispersion and Deposition of Fallout Particles from Sea-Water-Surface Nuclear Explosions, Report NRDL-TR-68-141 (AD-848308), Dec. 2, 1968.
7. G. K. Batchelor, Diffusion in a Field of Homogeneous Turbulence, *Aust. J. Sci. Res.*, 2A: 437 (1949).
8. T. V. Crawford, A Computer Program for Calculating the Atmospheric Dispersion of Large Clouds, USAEC Report UCRL-50179, Lawrence Radiation Laboratory, 1966.
9. E. C. Freiling, Fractionation. High-Yield Surface Burst Correlation, Report USNRDL-TR-385, U. S. Naval Radiological Defense Laboratory, Oct. 29, 1959; E. C. Freiling, Fractionation. Estimation of Degree of Fractionation and Radionuclide Partition for Nuclear Debris, Report USNRDL-TR-680, U. S. Naval Radiological Defense Laboratory, Sept. 12, 1963.
10. H. Bateman, The Solution of a System of Differential Equations Occurring in the Theory of Radioactive Transformations, *Proc. Cambridge Phil. Soc.*, **15**: 423 (1910).
11. D. K. Winegardner, PROFET: A Rapid Method for Generating Fallout Predictions from Field Data, Report NDL-TR-124 (AD-852969L), (Table 2.2), U. S. Army Nuclear Defense Laboratory, May 1969.
12. R. Wexler and D. Atlas, Moisture Supply and Growth of Stratiform Precipitation, *J. Meteorol.*, **15**: 531 (1958).
13. E. W. Kessler, On the Distribution and Continuity of Water Substance in Atmospheric Circulation, *Meteorol. Monogr.*, **10**(32) (November 1969).
14. L. R. Koenig, Parameterization of Ice Growth for Numerical Calculations of Cloud Dynamics, *Mon. Weather Rev.*, **100**: 417 (1972).
15. R. S. Sekhon and R. C. Srivastava, Snow Size Spectra and Radar Reflectivity, *J. Atmos. Sci.*, **27**: 299 (1970).
16. J. S. Marshall and W. McK. Palmer, The Distribution of Raindrops with Size, *J. Meteorol.*, **5**: 165 (1948).
17. W. S. Nordquist, Numerical Approximations of Selected Meteorological Parameters Related to Cloud Physics, Report TR-ECOM-5475 (AD-757623), U. S. Army Electronics Command, March 1973.
18. W. G. N. Slinn and J. M. Hales, Phoretic Processes in Scavenging, in *Precipitation Scavenging (1970)*, Richland, Wash., June 2–4, 1970, Rudolf J. Engelmann and W. George N. Slinn (Coordinators), AEC Symposium Series, No. 22 (CONF-700601), pp. 411-422, 1970.
19. W. G. N. Slinn and J. M. Hales, A Reevaluation of the Role of Thermophoresis as a Mechanism of In- and Below-Cloud Scavenging, *J. Atmos. Sci.*, **28**: 1465 (1971).
20. A. C. Chamberlain, Aspects of Travel and Deposition of Aerosol and Vapour Clouds, British Report AERE-HP/R-1261, Sept. 17, 1953.
21. R. J. Engelmann, The Calculation of Precipitation Scavenging, in Meteorology and Atomic Energy — 1968, D. H. Slade (Ed.), USAEC Report TID-24190, 1968.
22. G. B. Foote and P. S. duToit, Terminal Velocity of Raindrops Aloft, *J. Appl. Meteorol.*, **8**: 249 (1969).
23. I. Langmuir, The Production of Rain by a Chain Reaction in Cumulus Clouds at Temperatures Above Freezing, *J. Meteorol.*, **5**: 175 (1948).
24. M. P. Langleben, The Terminal Velocity of Snowflakes, *Quart. J. Roy. Meteorol. Soc.*, **80**: 174 (1954).

25. W. E. Ranz and J. B. Wong, Impaction of Dust and Smoke Particles on Surface and Body Collectors, *Ind. Eng. Chem.*, 44: 1371 (1952).
26. C. N. Davies, Definitive Equations for the Fluid Resistance of Spheres, *Proc. Phys. Soc. (London)*, 57: 259 (1945).
27. R. W. Perkins, C. W. Thomas, and J. A. Young, Application of Short-Lived Cosmogenic Radionuclides as Tracers of In-Cloud Scavenging Processes, *J. Geophys. Res.* 75: 3076 (1970).
28. N. H. Fletcher, *The Physics of Rain Clouds*, Cambridge University Press, 1966.
29. P. Squires, The Growth of Cloud Drops by Condensation, *Aust. J. Sci. Res.*, A5: 59 (1952).
30. J. E. McDonald, Cloud Nucleation on Insoluble Particles, *J. Atmos. Sci.*, 21: 109 (1964).
31. S. M. Greenfield, Ionization of Radioactive Particles in the Free Air, *J. Geophys. Res.*, 61: 27 (1956).
32. S. Twomey, The Nuclei of Natural Cloud Formation — Part II: The Supersaturation in Natural Clouds and the Variation of Cloud Droplet Concentration, *Geofis. Pura Appl.*, 43: 243 (1959).
33. N. F. Fletcher, Ice Crystal Production by Aerosol Particles, *J. Meteorol.*, 16: 173 (1959).
34. N. A. Fuchs, Evaporation and Droplet Growth in Gaseous Media, Izdatelstvo Akademii Nauk, SSSR, 1958; translation by J. M. Pratt under the editorship of R. S. Bradley (1960) is available from Pergamon Press, Inc., New York.
35. B. J. Mason, *The Physics of Clouds*, Table 3.1, p. 112, Clarendon Press, Oxford, 1971.
36. K. S. L. Gunn and J. S. Marshall, The Effects of Wind Shear on Falling Precipitation, *J. Meteorol.*, 12: 339 (1955).
37. M. W. Nathans, R. Thews, W. D. Holland, and P. A. Benson, Particle Size Distribution in Clouds from Nuclear Airbursts, *J. Geophys. Res.*, 75: 7559 (1970).

ADAPTATION OF A THREE-DIMENSIONAL ATMOSPHERIC TRANSPORT–DIFFUSION MODEL TO RAINOUT ASSESSMENTS

R. LANGE and J. B. KNOX
Lawrence Livermore Laboratory, University of California, Livermore, California

ABSTRACT

A hybrid Lagrangian–Eulerian atmospheric transport–diffusion model has been developed and validated for calculating the three-dimensional distribution of atmospheric pollutants in transient region flow fields. This code, ADPIC, has been validated against several existing closed-form analytical solutions including (1) a puff release in steady unidirectional shear flow and (2) a puff release with scale-dependent horizontal and vertical eddy-diffusion coefficients. These verification tests indicate that the ADPIC calculational method reproduced the standard deviation of the pollutant distribution within 5%. Regional tracer releases of methyl iodine at Idaho Falls also have been used to validate the capability of the code to estimate the regional distribution of the pollutant. These results are compared to measurements obtained by the National Oceanic and Atmospheric Administration (NOAA).

The ADPIC code for rainout assessments has been adapted to include radioactive decay and removal of debris from the cloud by wet-deposition processes. The changes in the surface radiation field due to explicit inclusion of speed and direction wind shear and time-dependent wet deposition for free-air-burst shots with a 1-kt yield are explored in a parameter-variation study.

In this paper we describe an emerging, validated capability for calculating the three-dimensional distribution of a nuclear aerosol after its downrange transport and diffusion to the site of a scavenging scenario or event. If the scavenging interaction takes place over an extended period of time, such as a half hour or more, the processes of transport and diffusion during that finite time of scavenging also need to be, and are, in fact, simulated by the capability we now describe. The numerical simulation model that serves this general purpose has been developed under funding by the AEC's Division of Biomedical and Environmental Research (DBER) in our Atmospheric and Geophysical Sciences Division. The numerical model to be described is known by the acronym ADPIC (*A*tmospheric *D*iffusion by *P*article *I*n-*C*ell).

To date, estimates of the potential hazard from the rainout of nuclear aerosols have been made without the explicit inclusion of either (1) the effects of wind shear deforming the cloud in space and time or (2) noninstantaneous deposition. We have deferred estimating the effects of these two factors on collateral damage in the research efforts at Lawrence Livermore Laboratory (LLL) until suitable tools are available. We feel that the worst rainout situation can now be calculated utilizing a tool such as ADPIC in a parametric study of the sensitivity of collateral damage to these effects and others.

During the period that a nuclear cloud has an overkill capability, i.e., while it can deliver doses far in excess of 150 rems, any process that spreads the cloud may lead to potentially greater collateral damage than that calculated so far by the vertical integral method. At least five parameters must be considered and varied over reasonable ranges in order to examine their effects on rainout deposition patterns. These parameters include vertical wind shear, the time of onset of rain, the intensity of the rain, the duration of the rain, and the rate of removal by the scavenging mechanism selected. The removal rates selected for the problems in this paper are 10^{-3} sec^{-1} and 10^{-4} sec^{-1}. As more is learned about precipitation interaction scenarios (including their seasonal variations) and about the spatial distribution of removal rates within natural cloud systems, it may be appropriate to examine other removal rates. It appears that the inclusion of a finite rain period, especially at early times, results in a substantial increase of the area of the 150-rad contour over that obtained using the vertical integral method. For example, the 150-rad contour area over a 1-kt debris cloud is increased by a factor of 2 with the inclusion of a 30-min rain period initiated at cloud stabilization.

Our study of the wet-deposition surface patterns for a standard 1-kt, free-air-burst, fission, nuclear debris cloud is divided into the following elements:

- A brief description of the formulation of the ADPIC code.
- A discussion of the verification of ADPIC solutions against closed-form analytical solutions.
- The validation of the ADPIC simulation against regional tracer studies at the Idaho Falls National Reactor Test Station (NRTS).
- The formulation of wet deposition in ADPIC.
- The wet-deposition patterns as a function of removal rate and directional and speed wind shear.

DESCRIPTION OF ADPIC

ADPIC is a hybrid, Lagrangian–Eulerian, three-dimensional, particle-in-cell code for calculating the transport and the anisotropic

diffusion of a pollutant from its source to its temporal and regional distribution at arbitrary times. ADPIC represents a convenient mathematical framework in which to include the following effects on a regional basis: speed and directional wind shear; occurrence of calms; space-variable surface roughness; wet and dry deposition; radioactive decay; gravitational settling; space- and time-dependent eddy diffusion parameters; and single or multiple sources of either continuous or instantaneous nature. ADPIC solves the three-dimensional advection diffusion equation in flux-conservative form using a pseudovelocity technique for a given regional mass-consistent advection field in three dimensions and in time.

In this method the Lagrangian particles represent the activity distribution and concentration associated with the nuclear aerosol within the structure of an Eulerian grid (the governing equations are shown in Fig. 1). The chief advantages of this ADPIC approach are (1) the artificial diffusion inherent in purely Eulerian finite-difference codes is practically eliminated and (2) the Lagrangian coordinates representing mass or activity can be tagged so that the age of each particle is known at all times.

Two versions of ADPIC have been developed. One version uses a fixed, regional Eulerian grid so that complex surface-boundary conditions may be incorporated in the solution. The second version uses an expanding grid that travels with the center of the pollutant cloud over flat terrain and automatically expands with the expanding cloud. The latter version is applicable to sensitivity studies in which a large number of parameters are varied. The grid spacing and the eddy diffusivity velocity algorithm used in ADPIC for the two-dimensional case is shown in Fig. 2.

Each ADPIC time cycle (Δt) consists of an Eulerian and a Lagrangian part. As shown in Fig. 3, in the Eulerian part the diffusivity velocity vector U_d and the pseudovelocity vector U_p are calculated as functions of the concentration field χ, the eddy diffusivity tensor K_d, and the mass-consistent regional flow field U_a. In the Lagrangian part the new position vector $\mathbf{R}$ for each Lagrangian particle is calculated from its old position vector plus the displacement of the particle in the pseudovelocity vector field U_p. It should be mentioned that the advective vector field U_a could be furnished externally by a regional, mass-consistent, objective-analysis code; a regional, predictive meteorological code; an urban heat-island simulation code; or a hydrodynamic model of a convective system. We have, of course, not achieved all of these objectives at this time and will report the results when a higher level of sophistication is achieved through inclusion of U_a input derived from regional, objective-analysis codes.

It is perhaps pertinent to explain briefly in a simple one-dimensional example the way in which the ADPIC formulation eliminates the fictitious

Advection diffusion equation:

$$\frac{\partial \chi}{\partial t} + U_A \cdot \nabla \chi = \nabla \cdot K_{ij} \nabla \chi$$

Assume:

$$\nabla \cdot U_A = 0 \qquad \text{(Incompressibility)}$$

Define:

$$U_D = -K_{ij} \frac{\nabla \chi}{\chi} \qquad \text{(Diffusivity velocity)}$$

Pseudovelocity form of diffusion-advection equation:

$$\frac{\partial \chi}{\partial t} + \nabla \cdot (U_P \chi) = 0$$

where $U_P = U_A + U_D$

and U_P is the pseudovelocity vector
U_A is the advection velocity vector
U_D is the diffusivity velocity vector
K_{ij} is the diffusivity tensor
χ is the concentration

Fig. 1 Governing equations for ADPIC.

diffusion plaguing the purely Eulerian finite-difference approach. In the upper portion of Fig. 4, we show the fate of a pollutant in a three-cell simulation of diffusive transport where all of the pollutant is initially (at T=0) in the first cell. At the end of a small time step (at T=1), a portion of the pollutant in the first box has been distributed to the second cell. In like manner, at the end of the second time step (at T=2), a portion of the pollutant has been transported to the third cell. During successive

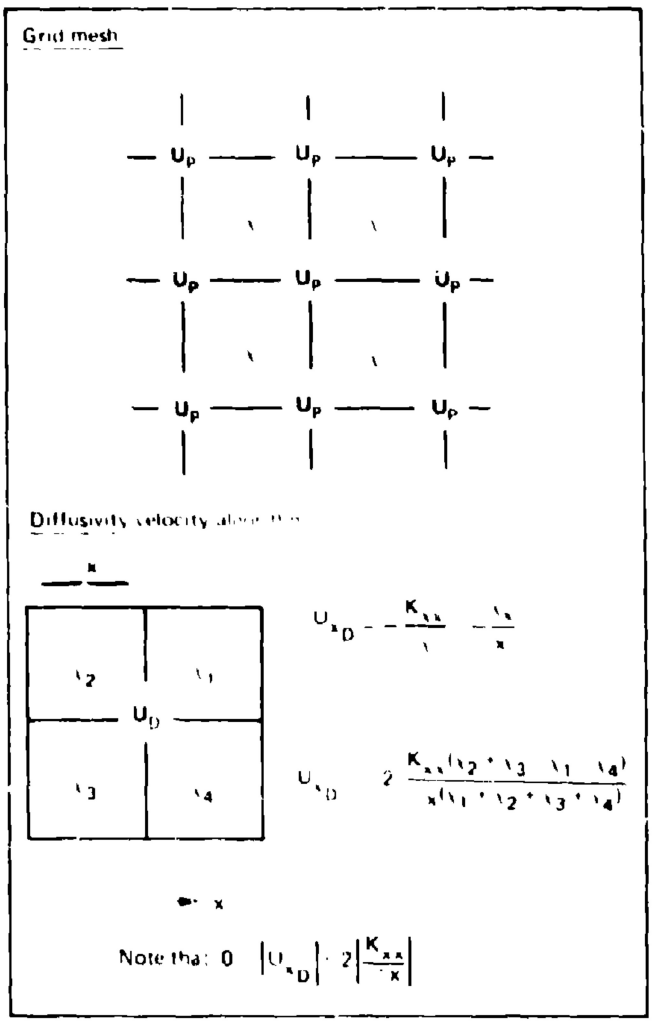

Fig. 2 Grid spacing and eddy diffusivity velocity algorithm used in ARPIC (two-dimensional example).

time steps, pollutant originating in the first cell is transmitted through the grid "too fast" because the pollutant in any cell with an adjacent empty cell is instantaneously shared. In contrast, the particle-in-cell treatment of diffusion moves each particle with the vector velocity U_p which incorporates the diffusive transport. The particles are seen in the lower part of Fig. 4 to move in a more physically consistent manner.

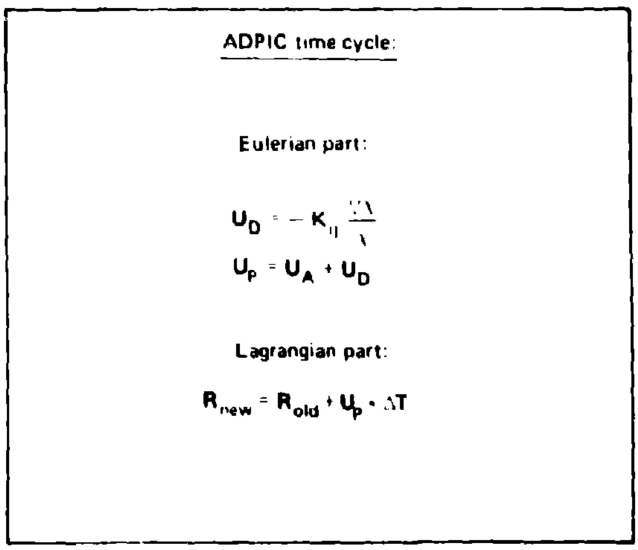

Fig. 5 ADPIC time cycle.

VERIFICATION OF ADPIC AGAINST ANALYTICAL SOLUTIONS

Verification of the ADPIC solution against the closed-form analytical solutions is summarized in Table 1. The standard deviation of the pollutant distribution was reproduced by the ADPIC solution within a maximum error of 5% and a mean error of 2% of the standard deviation for the analytical solution. The importance of this result is that the ADPIC code represents a reasonably accurate calculational framework for attacking regional transport–diffusion problems for transient regional flow fields in multi-dimensional space. In addition, for most applications the accuracy of the method appears to be sufficiently high, and the residual errors are normally small in comparison to our knowledge of the source term. The quality of the ADPIC solutions, therefore, is governed by our knowledge of the temporal–spatial regional flow fields and the spatial distribution and time dependency of the eddy diffusion processes.

We now proceed to discuss in some detail the validation for Cases 2 and 3 of Table 1 as performed by the automatically expanding-grid version of ADPIC. (Cases 1 and 4 to 6 are discussed in Ref. 1.) Validation Case 2 is the instantaneous source for scale-dependent diffusion in the two-dimensional mode in which we evoke some 14×14 cells in the x,y plane and depict the distribution of particles by 3168 Lagrangian marker particles which are subject to the scale-dependent diffusion formulation provided by Walton.[4] The upper panel of Fig. 5 shows the

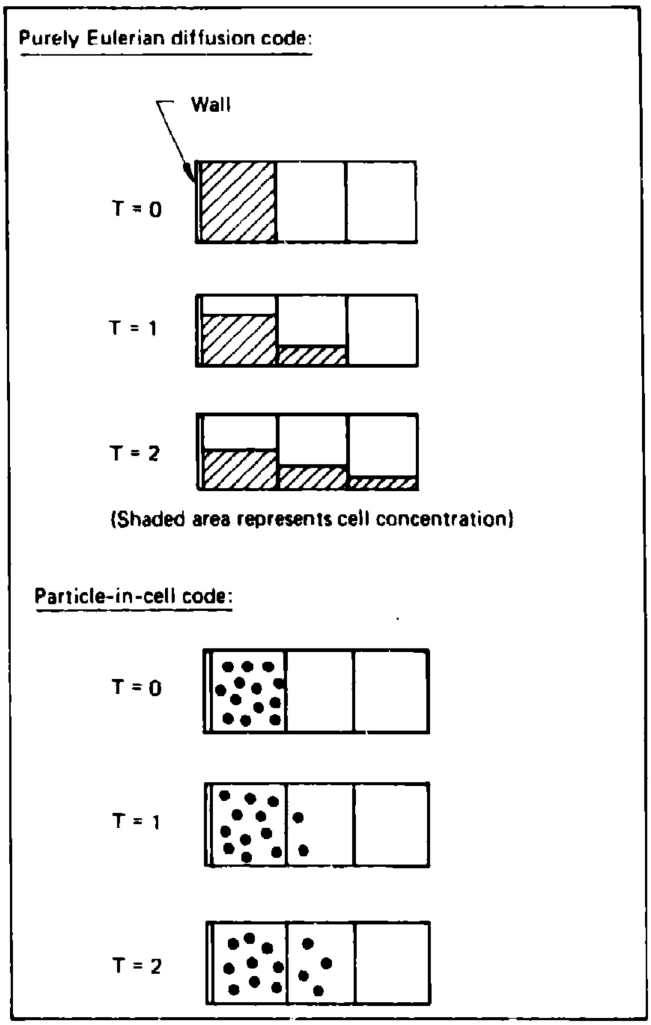

Fig. 4 Simplified illustration of the elimination of the fictitious diffusion in ADPIC.

initial distribution of the pollutant in the y,z plane as depicted by the ADPIC code and by the analytical solution. The lower panel of Fig. 5 shows the distribution of pollutant in an unbounded y,z plane with the small rectangle in the center of the panel depicting the calculation grid. The initial distribution of the pollutant in two-dimensional space is shown inside the calculational grid by Lagrangian marker particles.

Figure 6 displays the same information after the passage of 88,720 sec and compares the ADPIC solution to the analytical solution in the

TABLE 1

ADPIC VERIFICATION AGAINST CLOSED GAUSSIAN SOLUTIONS

For initially Gaussian, instantaneous, and continuous sources, ADPIC has been found to agree with analytical solutions to the diffusion-advection equation to within 5% of the standard deviation for the following cases:

Case	Description
1	Instantaneous source; constant-K diffusion
2	Instantaneous source; scale-dependent K(t) diffusion
3	Instantaneous source; constant-K diffusion in simple vertical speed shear $U = U(z)$, $V = W = 0$
4	Continuous source; constant-K diffusion
5	Continuous source; constant-K diffusion; advection = U = 2 m sec^{-1}
6	Continuous source; constant-K diffusion; advection = U = 10 m sec^{-1}

upper panel in the y,z plane. The actual spatial distribution in the y,z plane is shown in two-dimensions in the lower panel after anisotropic diffusion has converted the cloud into a thin, horizontal, pancake-shaped cloud due to the fact that the scale-dependent diffusion coefficient operating the y dimension far exceeds that of the vertical eddy-diffusion coefficient.

Figure 7 shows the cloud-center concentration as a function of time for both the analytical solution and the ADPIC solution up to approximately 100,000 sec. Note from Fig. 6 that the tails of the distribution and the magnitude of the peak concentration are correctly calculated and are essentially free of the fictitious diffusion processes that have contaminated previous diffusion calculations which were done in a purely Eulerian framework.

Validation Case 3 is that for an instantaneous point source having constant diffusion coefficients and incorporating a strong, simple, vertical wind-speed shear in three-dimensional space. We utilize 20 cells in each dimension x,y,z and depict the initial distribution of the spherically symmetric Gaussian cloud by some 10,000 Lagrangian marker cells. Figure 8 displays the distribution of Lagrangian marker cells at approximately 5 sec in the x,z plane in unbounded shear flow.

The upper panel of Fig. 9 compares the analytical solution and the ADPIC solution of the number of particles per cell as a function of distance in the x,z plane at approximately 6300 sec. The panel in the lower part of Fig. 9 shows the distribution of the pollutant after deformation transport and diffusion in the unbounded shear flow. Figure 10 shows relative cloud-center concentration as a function of time for the shear-flow case.

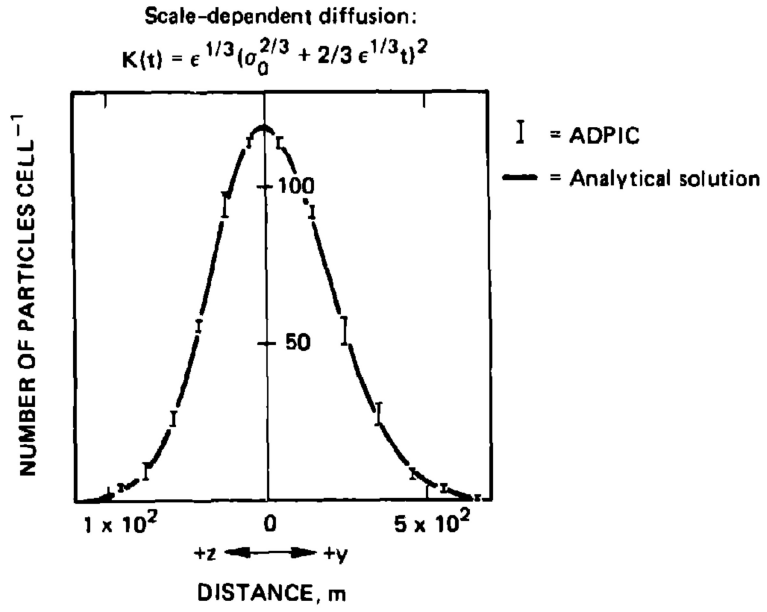

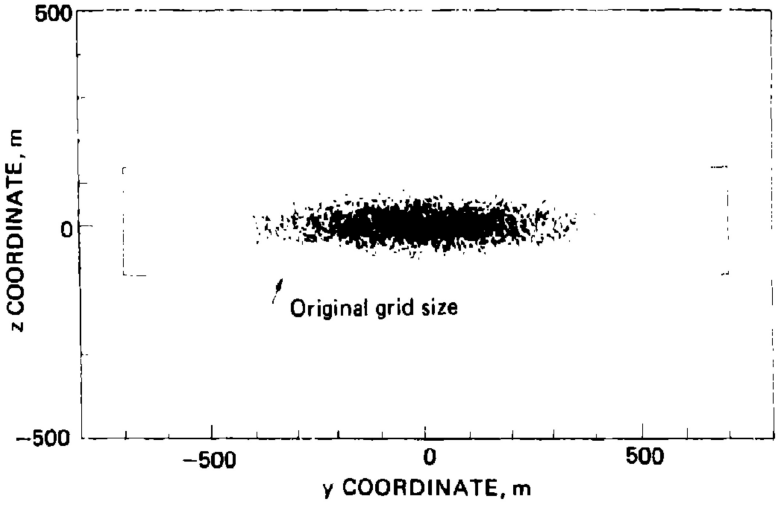

Fig. 5 Scale-dependent diffusion: initial distribution.

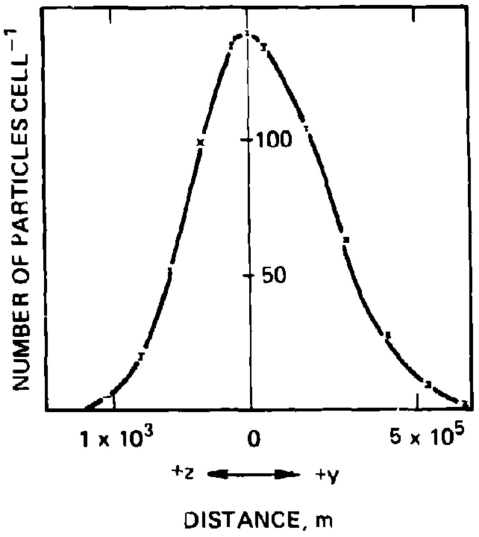

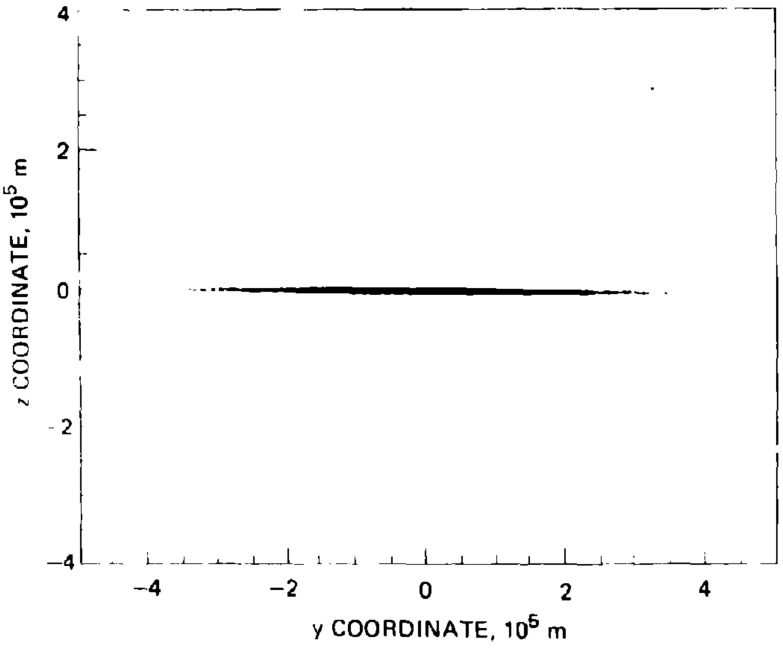

Fig. 6 Scale-dependent diffusion: distribution after 38,720 sec.

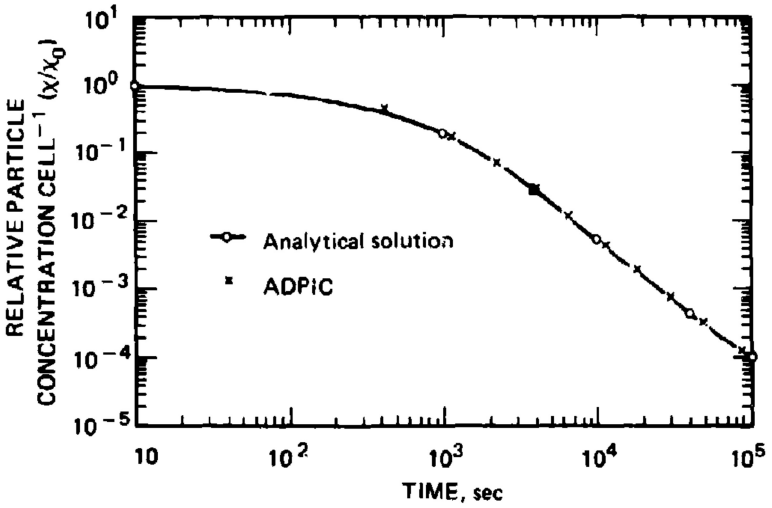

Fig. 7 Scale-dependent diffusion: plot of relative particle concentration per cell at cloud center vs. time.

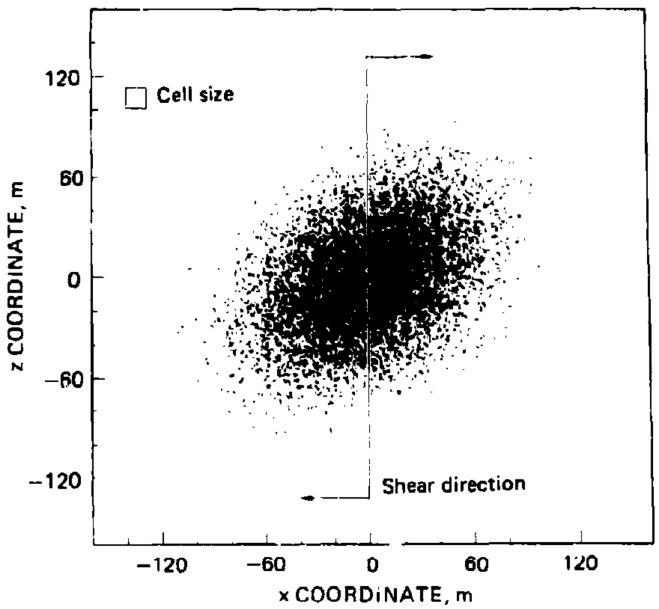

Fig. 8 Diffusion in shear flow: particle distribution at cycle 20, $t = 5.3$ sec, x,z plane.

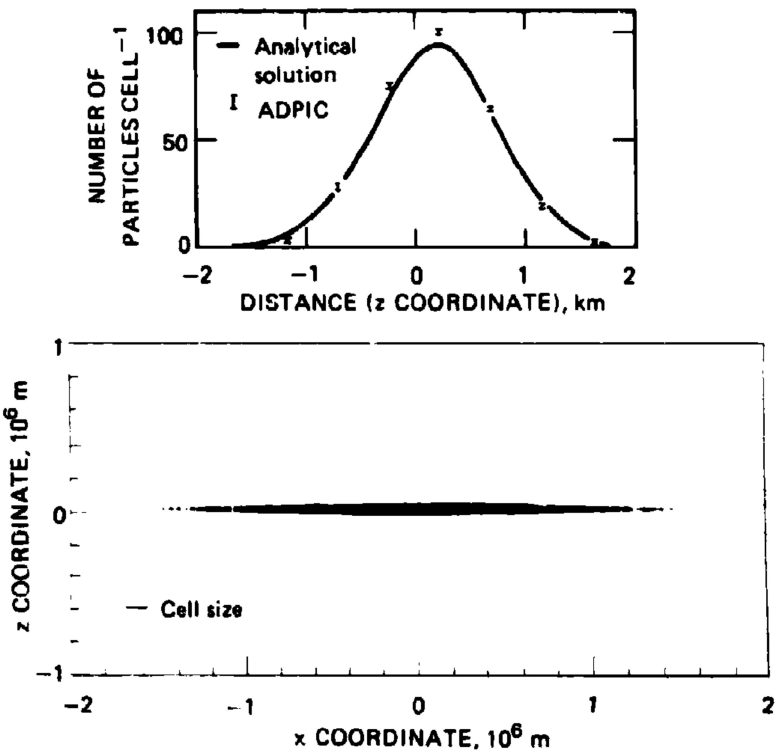

Fig. 9 Diffusion in shear flow: particle distribution at cycle 120, t = 6328 sec, x,z plane.

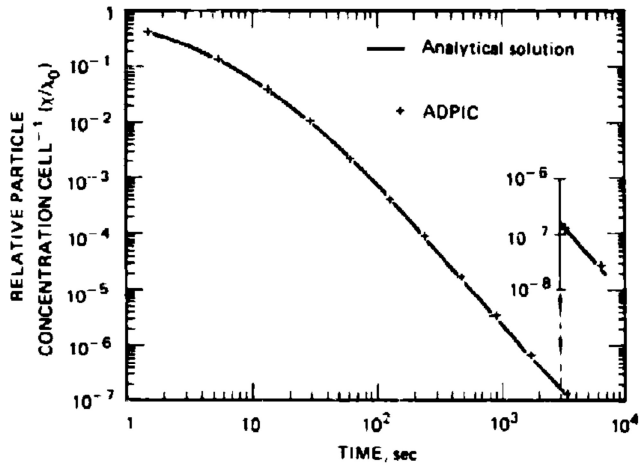

Fig. 10 Diffusion in shear flow: relative cloud center concentration vs. time.

The two validation studies comparing the ADPIC solutions to closed analytical solutions depict in a representative way the calculational capability of this code to treat anisotropic diffusion of pollutants in stratified shear flow.

VALIDATION OF ADPIC AGAINST A REGIONAL TRACER STUDY AT THE IDAHO FALLS NRTS SITE

For the past few years, the NOAA has performed regional tracer tests at the Idaho Falls National Reactor Test Station (NRTS). The NRTS staff at that location provided both the meteorological and source-term information for one of their methyl iodine releases. That test consisted of a 3-hr injection of methyl iodine with ^{131}I into a transient regional flow field. Meteorological properties were documented by 17 meteorological towers as well as by upper-level wind measurements. In addition, 36 field samplers were arranged in four arcs at various distances downwind from the source.

The regional flow field was calculated by the LLL three-dimensional, mass-consistent, wind-field code MATHEW.[3] Its output for several hours after release describes the regional flow field needed for the atmospheric transport–diffusion calculations. ADPIC was used to simulate each sampler on each arc by counting the particles passing through a sampler cell volume as a function of time. Thus ADPIC simulated the time history of the passage of the cloud over each of the samplers while also calculating the total spatial-temporal distribution of the pollutant. The details of the ADPIC problem setup and a summary of the results are included in Table 2.

TABLE 2

VALIDATION OF ADPIC AGAINST FIELD TRACER STUDY AT NRTS, IDAHO FALLS

Problem setup:

- Number of grid cells: 16 × 24 × 24 = 9216
- Vertical cell size = 50 m; horizontal cell size = 4300 m
- Stability category: Pasquill C
- Source release rate = 0.379 mCi sec^{-1} for 3 hr. At 0.25 mCi particle^{-1}, this corresponds to 14,720 particles total
- Deposition velocity = 0.1 cm sec^{-1}

Comparison between ADPIC and field-sampler results:

Agreement within factor of:	2	5	10
Fraction of total samples $\left(\frac{\text{ADPIC samplers}}{\text{field samplers}}\right)$	0.44	0.81	0.89

As an aid to interpreting the results, Fig. 11 shows the complex topography of the Idaho Falls region and the general outline of the plume as it was transported downwind from its source. The same topographic boundary conditions have been used in both the regional flow-field model and in the solution of regional transport diffusion by ADPIC. These boundary conditions are depicted in this figure. The spatial distribution of the methyl iodine cloud at 1 hr is shown in Fig. 12 by means of a projection of each of the Lagrangian particles onto the horizontal plane; sampling arcs A, B, C, and D are shown as large dots. The region of calculation by the ADPIC code is also indicated.

Figure 13 shows the horizontal projection of the same Lagrangian marker particles representing the cloud onto the x,y plane at 3 hr. Embroidery along the left side of the pollutant cloud is introduced by topography. A simulated ADPIC surface-air concentration history at sampler A-3 is shown in Fig. 14 and is compared in terms of its breadth to the actual passage time of the plume as documented by field measurements.

Figures 15 to 17 show the integrated concentration at the samplers along arcs B, C, and D as a function of crosswind distance. Field data points with arrows indicate threshold values of instruments. In Fig. 16 the observed integrated concentrations are compared to the results obtained by solutions using the standard, bivariant, Gaussian, plume equations for the stability categories C and D. Note that, although one of the Gaussian solutions matches the peak concentration at what might be construed to be the plume axis, the general breadth of the pattern is badly missed, errors of two or more orders of magnitude occur on the left and right flanks, and the second peak cannot be accounted for by the simple Gaussian plume model. We interpret this to be a result of the effects of regional directional wind shear and transient regional flow on the distribution of the pollutant. As can be seen from Table 2, ADPIC in fact predicts the breadth of the plume reasonably correctly, with 44% of the points being within a factor of 2 of those observed and 80% being within a factor of 5.

We interpret the sources of error in ADPIC matching as follows: The principal sources of error result from the objective prescription of the regional flow field, the state-of-the-art prescription of eddy-diffusion coefficients as a function of bulk meteorological variables, and the sensitivity of the surface-air concentration to simplifications made in representing topography in the MATHEW and ADPIC formulations. It should be clear that these sources of error far exceed the sources of error discussed in the comparison of the ADPIC code capability to the analytical solutions discussed under the heading "Verification of ADPIC Against Analytical Solutions."

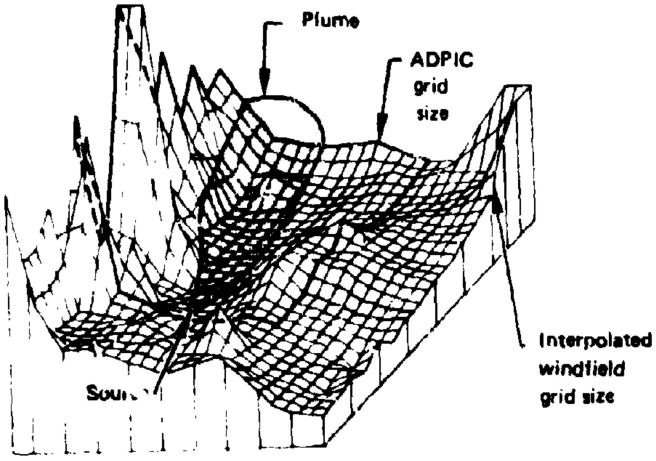

Fig. 11 Idaho Falls topography and plume outline.

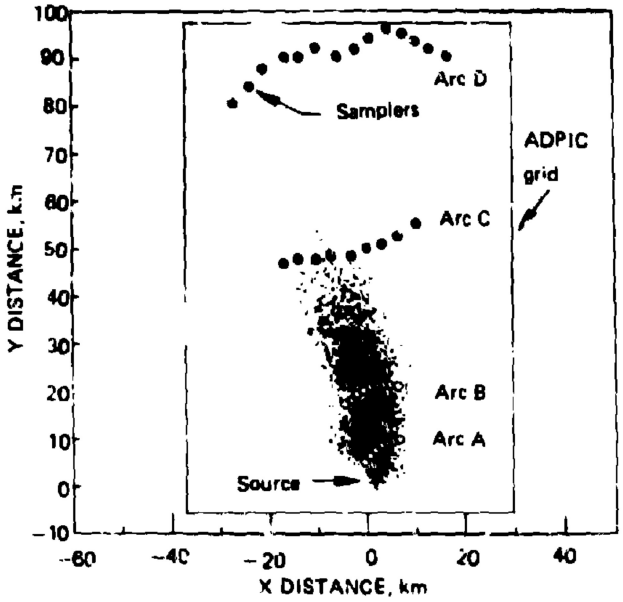

Fig. 12 Idaho Falls plume after 1 hr.

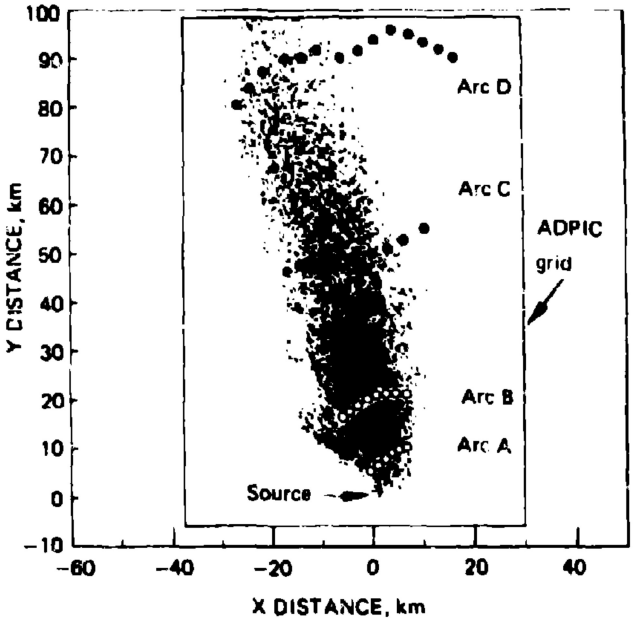

Fig. 13 Idaho Falls plume after 3 hr.

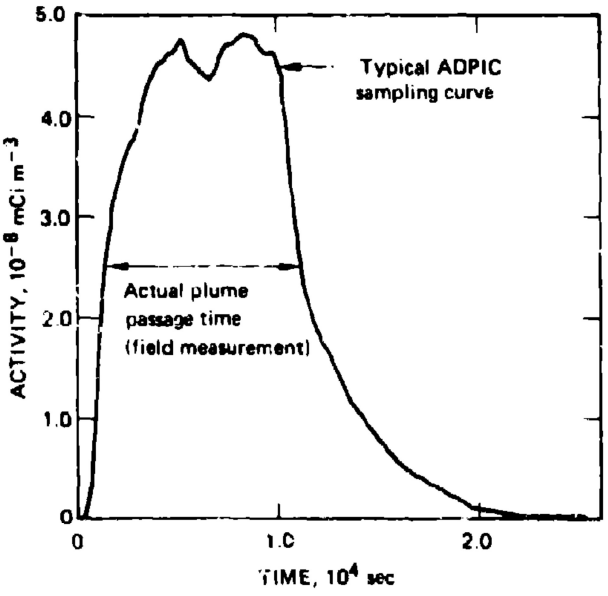

Fig. 14 Activity vs. time for simulated ADPIC sampler A-3.

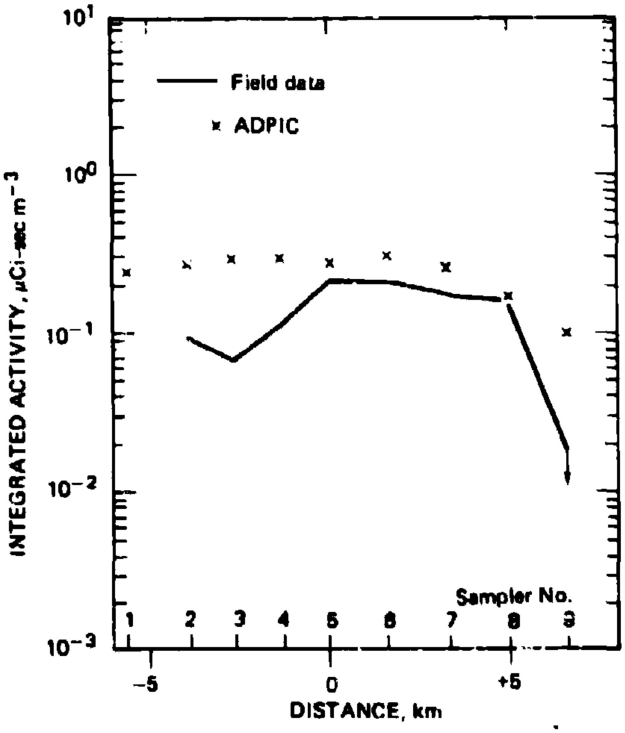

Fig. 15 Integrated activity for samplers on arc B.

FORMULATION OF ADPIC WET-DEPOSITION MECHANISMS

Precipitation scavenging by hydrometeors whose growths have substantially terminated is treated as follows in ADPIC. For a specified rain rate prevailing over a given surface area, a washout coefficient, $\Lambda(r)$, is assumed as a function of debris particles of size r. Because of their limited number, each ADPIC particle is much larger than a debris particle. Therefore an ADPIC mass particle is initially considered to represent an integrated distribution of debris particles over sizes such that

$$M(0) = \int_{r=0}^{\infty} m(r, 0)\, dr$$

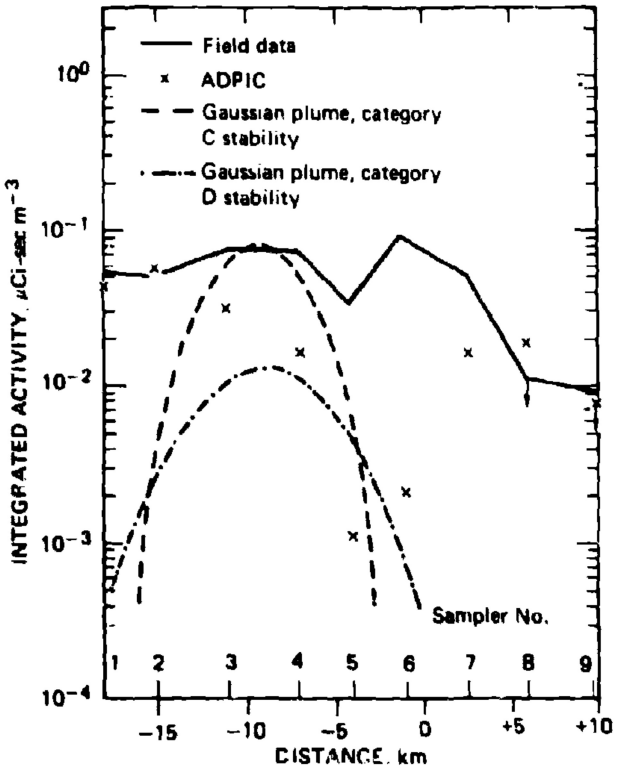

Fig. 16 Integrated activity for samplers on arc C.

where M(0) is the initial mass of an ADPIC particle and m(r, 0) is the mass per [illegible] of [illegible] particle of radius r at time 0. Constant density is assumed for the debris particles. M(t), the mass of an ADPIC particle remaining after a time t in the rain for a given constant rain rate and raindrop size distribution, can then be written as[4]

$$M(t) = \int_{r=0}^{\infty} m(r, t)\, dr$$

$$= \int_{r=t}^{\infty} m(r, 0) e^{-\lambda(r)t}\, dr$$

To account for the diffusion and transport of pollutant as calculated by ADPIC, this function M(t) is computed (or looked up from a table) at each ADPIC time step, Δt. The fraction of mass, F(Δt), of an ADPIC

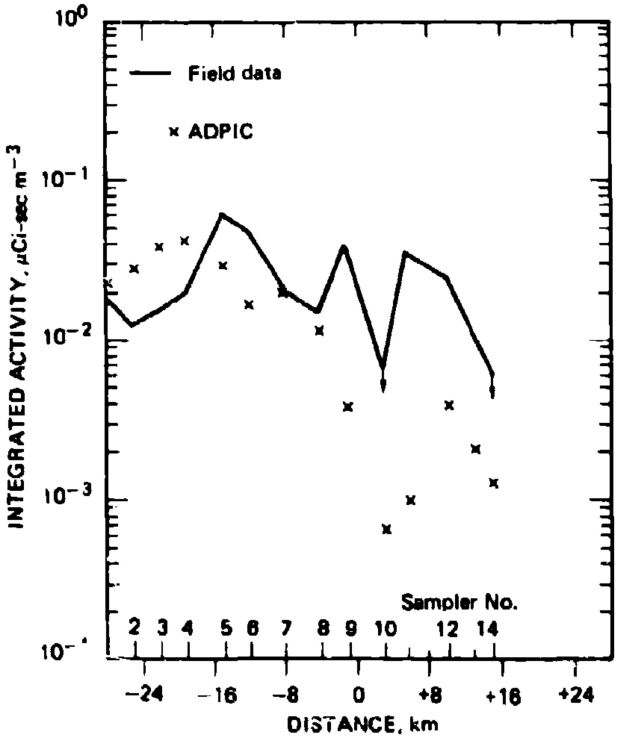

Fig. 17 Integrated activity for samplers on arc D.

particle washed out and deposited on the surface during one ADPIC time cycle then becomes

$$F(\Delta t) = \frac{M(t) - M(t + \Delta t)}{M(t)}$$

$$1 - \frac{\int_{r=0}^{\infty} m(r, 0)e^{-\Lambda(r)t+\Delta t)}\, dr}{\int_{r=0}^{\infty} m(r, 0)e^{-\Lambda(r)t}\, dr}$$

This fraction of mass loss per cycle for each ADPIC particle is cumulatively stored after each cycle in a two-dimensional, surface-deposition array.

WET-DEPOSITION PATTERNS AS A FUNCTION OF RAIN RATE OR REMOVAL RATE AND DIRECTIONAL AND SPEED WIND SHEAR FOR 1-kt, FISSION, DEBRIS CLOUDS

For studying rainout from stabilized debris clouds following trajectories over long distances and time, the moving, automatically expanding grid version of ADPIC is used. This ensures uniform resolution of the cloud by the grid over many orders of magnitude of cloud growth.

In the following survey, ADPIC is used to examine the effects of instantaneous vs. noninstantaneous rainout under no shear, speed shear, and speed plus directional shear conditions on a 1-kt, fission cloud at both early and late time. Table 3 describes the parameters of the problem.

TABLE 3

DESCRIPTION OF THE 1-kt, FISSION PROBLEM

Number of ADPIC cells = $20 \times 20 \times 20$
Number of particles = 11,000
Initial cloud center height = 3000 m
Initial cloud thickness* = 1860 m
Initial cloud radius* = 950 m
} at stabilization time H + 600 sec
Yield = 1 kt at H + 1 hr
Radioactive decay $\propto t^{-1.2}$ (t in hr)
Mean advection velocity = 11 m sec^{-1}
Speed shear $dU/dz = 0.0015$ sec^{-1}
Directional shear $dV/dz = 0.001$ sec^{-1}
Horizontal scale-dependent diffusion $K_h = \epsilon^{1/3}(\sigma_y^{4/3} + \frac{1}{15}\epsilon^{1/3}t)^3$ m^3 sec^{-1}
with $\epsilon = 10^{-4}$ m^2 sec^{-3}
Vertical diffusion $K_z = 0.1$ m^2 sec^{-1}
Rain rates $\Lambda = \infty$, 0.001 sec^{-1}, and 0.0001 sec^{-1}
Rainout over the entire cloud
Rainout times† t = 0–1800 sec and 3600–5400 sec

* Corresponds to two standard deviations from cloud center.
† t = 0 corresponds to stabilization time H + 600 sec.

A summary of the survey problems and the results is shown in Table 4. Note that the instantaneous vertical integral was calculated at the mean time of arrival defined as the midpoint of the rain period.

Figures 18 to 20 show the wet-deposition patterns on the ground in isopieths for infinite dose from mean time of arrival for various rain rates and shear conditions for an early rain time from t = 0 to t = 1800 sec.‡ Problem A, Fig. 18, is the instantaneous total vertical integral at mean rain time of 900 sec without any shear. Problem B in the same figure

‡ t = 0 refers to the time at which the cloud stabilizes.

TABLE 4

SURVEY PROBLEMS AND RESULTS FOR 1-kt RAINOUT

Problem no.	Speed shear (dU/dz), sec^{-1}	Directional shear (dV/dz), sec^{-1}	Λ, sec^{-1}	Rain period*, sec, start/stop	Peak dose†, $rads_x$	Fraction of‡ initial activity remaining after rainout	Approximate area§ inside 150-rad contour, km^2
A	—	—	∞§§	900/900	11,000	0	12
B	—	—	10^{-3}	0/1800	7,700	0.2	20
C	0.0015	—	10^{-3}	0/1800	7,700	0.2	21
D	0.0015	0.001	10^{-3}	0/1800	7,700	0.2	21
E	—	—	∞§§	4500/4500	850	0	78
F	—	—	10^{-3}	3600/5400	480	0.01	66
G	0.0015	—	10^{-3}	3600/5400	450	0.01	68
H	0.0015	0.001	10^{-3}	3600/5400	350	0.01	68
I	0.0015	0.001	10^{-4}	0/1800	830	0.7	13
J	0.0015	0.001	10^{-4}	3600/5400	50	0.4	0

* From stabilization time H + 600 sec.
† Infinite dose from mean time of arrival.
‡ Initial activity defined as $4.4 \times 10^{+8}$ Ci at H + 1 hr.
§ Estimated from contour plots.
§§ Instantaneous vertical integral.

shows the effect of noninstantaneous deposition over ½ hr with a rain rate of $\Lambda = 10^{-3}$ sec^{-1}, again with no shear. Problems C and D in Fig. 19 show the additional effect of speed shear only and of speed plus directional shear. Problem I, Fig. 20, is the same as Problem D but with a rain rate of $\Lambda = 10^{-4}$ sec^{-1}.

Figures 21 to 23 (problems E, F, G, H, and J) show deposition patterns for a 30-min rain period at a later time (from t = 3600 to t = 5400 sec) for the same variation of parameters of rain rate and shear as for the early rain period discussed above.

CONCLUSION

Table 4 summarizes results as a function of rain period and rain rate for all of the problems run in terms of peak infinite dose, fraction of H + 1 activity remaining after the rain stops, and approximate area inside the 150-rad_x contour. In general and within the limitations of this parameter study, one can say that:

- Shear effects are minimal at early times but become significant at later times in terms of lowering peak dose, increasing the overall total area, and altering the shape of the entire deposition pattern. For a 1-kt cloud, the increase of the 150-rad_x contour area is not

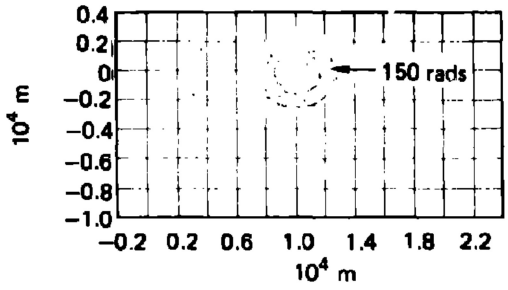

Problem A:
$\Lambda = \infty$: no shear; total vertical integral at T = 900 sec: isopleths for 1500, 150, 15, and 1.5 rads$_\infty$.

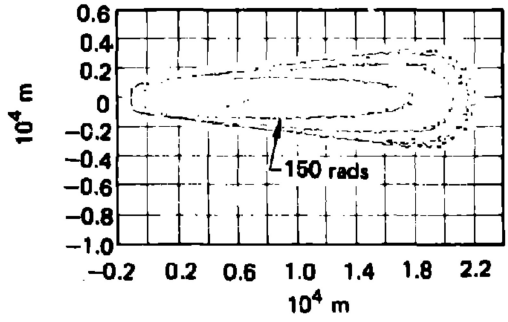

Problem B:
$\Lambda = 10^{-3}$ sec^{-1}; no shear; rain time t = 0–1800 sec (from stabilization); isopleths for 1500, 150, 15, and 1.5 rads$_\infty$.

Fig. 18 Isopleths of infinite dose from mean time of arrival for problems A and B.

as critical at periods of 1 hr or later because the peak dose is no longer much higher than the 150-rad$_\infty$ level. For a larger yield, this increase in area could be critical.

- Finite rain periods increase the areas of equal-dose isopleths over those obtained from instantaneous, full vertical integral deposition at a time equal to the mean rain time. This effect is most pronounced at early times, where an increase of about a factor of 2 is found.
- The shape of the dose isopleths is strongly affected by shear and by when the rain period occurs. Typically, early-dose (t = 0 to t = 1800 sec) isopleths tend to be cigar-shaped, whereas later time (t > 3600 sec) isopleths are more circular.
- Inclusion of shear effects and finite rainout periods in the ADPIC

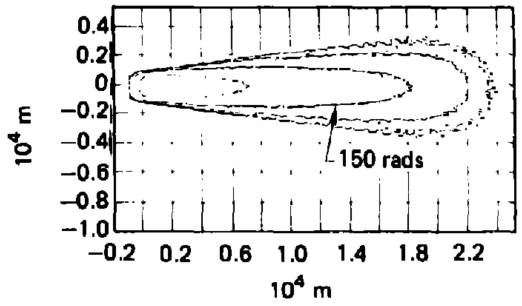

Problem C:
$\Lambda = 10^{-3}$ sec^{-1}; dU/dz = 0.0015 sec^{-1}; dV/dz = 0; rain time t = 0–1800 sec; isopleths for 1500, 150, 15, and 1.5 rads$_\infty$.

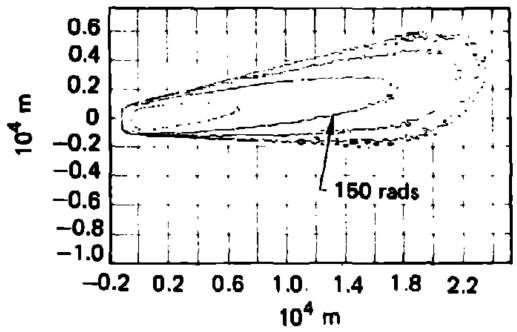

Problem D:
$\Lambda = 10^{-3}$ sec^{-1}; dU/dz = 0.0015 sec^{-1}; dV/dz = 0.001 sec^{-1}; rain time t = 0–1800 sec; isopleths for 1500, 150, 15, and 1.5 rads$_\infty$.

Fig. 19 Isopleths of infinite dose from mean time of arrival for problems C and D.

rainout calculations appears to be essential in determining a worst case. For example, comparison between Problem H (Fig. 22) with Problem I (Fig. 20) indicates that, in terms of the area inside the 150-rad$_\infty$ isopleths, a later rain period at a higher rain rate may be much worse than an early rain period at a lower rain rate.

ACKNOWLEDGMENT

This work was performed under the auspices of the U. S. Atomic Energy Commission and under the sponsorship of the Defense Nuclear Agency (Contract IACRO-73-814).

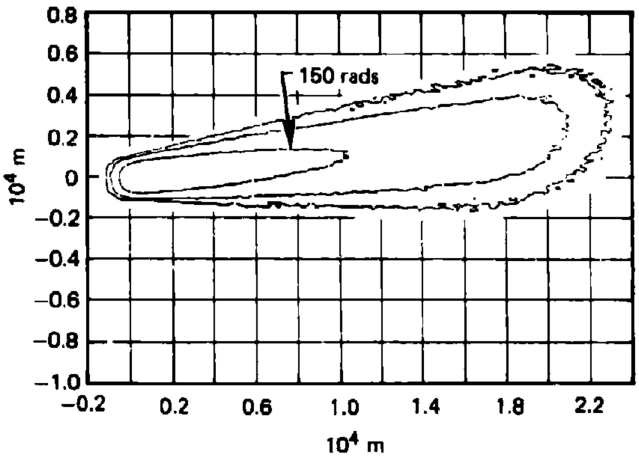

Problem I:
$\Lambda = 10^{-4}$ sec^{-1}; dU/dz = 0.0015 sec^{-1}; dV/dz = 0.001 sec^{-1}; rain time t = 0–1800 sec; isopleths for 150, 15, and 1.5 rads.

Fig. 20 Isopleths of infinite dose from mean time of arrival for problem I.

REFERENCES

1. R. Lange, A Three-Dimensional Computer Code for the Study of Pollutant Dispersal and Deposition Under Complex Conditions, Lawrence Livermore Laboratory Report UCRL-51462, 1963.
2. J. J. Walton, *J. Appl. Meteorol.*, 12: 547 (1973).
3. J. B. Knox, M. H. Dickerson, R. Lange, P. N. Gresho, and C. A. Sherman, Methods of Calculating Atmospheric Transport and Diffusion, Lawrence Livermore Laboratory (to be published as a UCRL report).
4. W. K. Crandall, C. R. Molenkamp, A. L. Williams, M. M. Fulk, R. Lange, and J. B. Knox, An Investigation of Scavenging of Radioactivity from Nuclear Debris Clouds: Research in Progress, Lawrence Livermore Laboratory Report UCRL-51328, 1973.

DISCUSSION

Norment: I understand that the complete wind field is derived from observed data via a variational method that ensures satisfaction of continuity. How is the diffusivity tensor field obtained? Has sensitivity to variation of the diffusivity tensor been studied?

Lange: While ADPIC can accommodate the entire V_{ij} tensor, the Idaho Falls study was basically done with obtaining only the diagonal K_{ii} terms from Pasquill type H ability categories in a parametric representation.

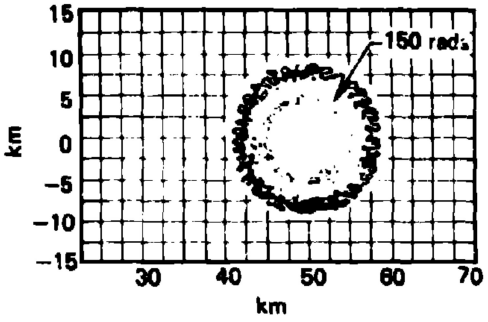

Problem E:
$\Lambda = \infty$; no shear; total vertical integral at T = 4500 sec; isopleths for 150, 15, and 1.5 rads$_{\infty}$.

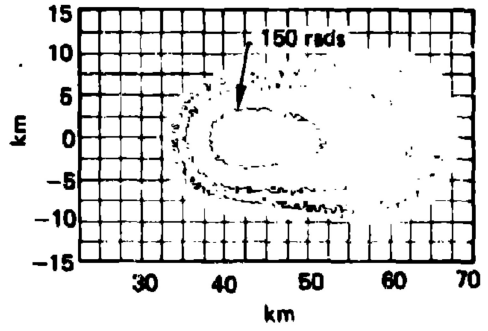

Problem F:
$\Lambda = 10^{-3}$ sec^{-1}; no shear; rain time t = 3600–5400 sec; isopleths for 150, 15, and 1.5 rads$_{\infty}$.

Fig. 21 Isopleths of infinite dose from mean time of arrival for problem E and F.

Beard: Would you comment on the updating of the wind field in the Idaho Falls simulation? Aren't the results highly sensitive to the errors in the wind field?

Lange: Yes they are.

Slinn: Besides commenting on the desirability that you use either vector or Cartesian tensor notation for V_D but not a mix, I would like to hear your response to the following potential. Criticisms (1) Why use K-theory rather than mixing velocities for an unstable atmosphere since you have the velocity field specified? (2) For stable cases why use K-theory when for large time the uncertainties in the advection field will almost certainly dominate the uncertainties in the spatial distribution

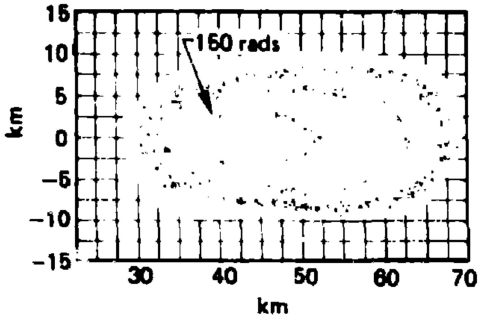

Problem G:
$\Lambda = 10^{-3}$ sec^{-1}; $dU/dz = 0.0015$ sec^{-1}; $dV/dz = 0$; rain time t = 3600–5400 sec; isopleths for 150, 15, and 1.5 rads.

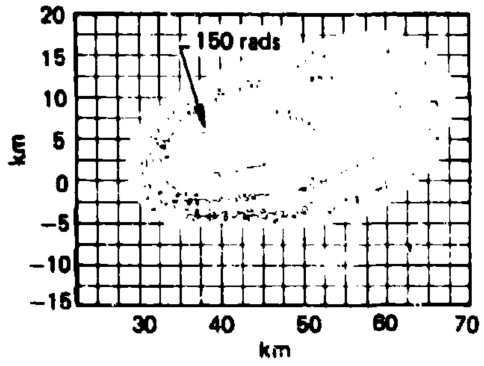

Problem H:
$\Lambda = 10^{-3}$ sec^{-1}; $dU/dz = 0.0015$ sec^{-1}; $dV/dz = 0.001$ sec^{-1}; rain time t = 3600–5400 sec; isopleths for 150, 15, and 1.5 rads.

Fig. 22 Isopleths of infinite dose from mean time of arrival for problems G and H.

of χ. It is of course significant that if K-theory is then abandoned, much less computer time will be necessary.

Lange: (1) To obtain the diffusion coefficients one needs an eddy velocity fluctuation and a scale length. If I understand your term mixing velocity to be a velocity fluctuation of the mean velocity field it would not be sufficient to provide diffusion coefficients. I am not sure that knowledge of the gradients of the *given mean* velocity field can be used to obtain fluctuation velocities or diffusion parameters.

(2) In our joint program with the Savannah River Laboratory in Aiken, S. C., we have run across data of plumes under stable conditions

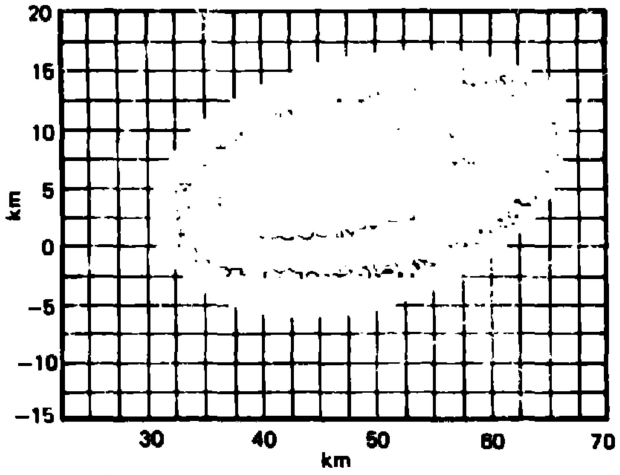

Fig. 23 Isopleths of infinite dose from mean time of arrival for problem J.

where changes in the advection field did not dominate the diffusion. Perhaps it should be pointed out in our paper that, while ADPIC is capable of accommodating the entire diffusivity tensor K_{ij}, in practice it uses to date only the diagonal terms k_{ii} in conventional formulation derived from stability categories, scale length arguments, Richardson's number, etc. Your criticism is valid that a full K-theory treatment is not likely to be necessary for the NRTS Idaho Falls type of study.